

1 Dynamics of wind-affected volcanic plumes: the example of 2 the 2011 Cordón Caulle eruption, Chile

3
4 ¹C. Bonadonna, ²M. Pistolesi, ²R. Cioni, ³W. Degruyter, ⁴M. Elissondo, ⁴V.
5 Baumann

6
7 ¹, Section des sciences de la Terre et de l'environnement, Université de Genève, Suisse

8 ², Dipartimento di Scienze della Terra, Università di Firenze, Italia

9 ³, Earth and Atmospheric Sciences, Georgia Tech, USA

10 ⁴, Servicio Geológico Minero Argentino, Argentina

11

12 **Abstract**

13 The 2011 Cordón Caulle eruption represents an ideal case study for the characterization of
14 long-lasting plumes that are strongly affected by wind. The climactic phase lasted for about
15 one day and was classified as subplinian with plumes between ~9-12 km above the vent
16 and Mass Flow Rate (MFR) on the order of $\sim 10^7$ kg s⁻¹. Eruption intensity fluctuated during
17 the first 11 days with MFR values between 10^6 - 10^7 kg s⁻¹. This activity was followed by
18 several months of low-intensity plumes with MFR $< 10^6$ kg s⁻¹. Plume dynamics and rise were
19 strongly affected by wind during the whole eruption with negligible up-wind spreading and
20 sedimentation. The plumes developed on June 4-6 and 20-22 can be described as
21 transitional plumes, i.e. plumes showing transitional behavior between strong and weak
22 dynamics, while the wind clearly dominated the rise height on all the other days resulting
23 in the formation of weak plumes. Individual phases of the eruption range between VEI 3-4,

24 while the cumulative deposit related to June 4-7, 2011, is associated with a VEI 4-5.
25 Crosswind cloud and deposit dispersal of the first few days are best described by a linear
26 combination of gravitational spreading and turbulent diffusion, with velocities between 1-
27 10 m s⁻¹. Downwind cloud velocity for the same days is best described by a linear
28 combination of gravitational spreading and wind advection, with velocities between 17-45
29 m s⁻¹. Results show how gravitational spreading can be significant even for subplinian and
30 small-moderate eruptions strongly advected by wind and with low Richardson number and
31 low MFR.

32

33 Keywords: Eruption classification; Mass Eruption Rate; cloud spreading; plume dynamics;
34 turbulent diffusion; density-driven transport

35

36 **1. Introduction**

37 Fundamental volcanic processes, such as conduit and plume dynamics, abrupt
38 transitions in eruptive regimes and eruption unsteadiness, are currently only partially
39 understood. This generates confusion in the way we characterize and classify eruptions,
40 especially in the cases of small-moderate eruptions, and hinders our capability to identify
41 potential eruptive scenarios and assess the associated hazards. The characterization and
42 classification of volcanic eruptions is crucial to: i) our scientific understanding (i.e. to
43 simplify a complex system by identifying leading-order processes and to aid comparison
44 between different eruptions or volcanoes); ii) hazard and risk assessment; and iii) science
45 and hazard communication [Bonadonna et al., 2014]. Nonetheless, most existing
46 classification schemes only include parameters that do not represent the full complexity of
47 volcanic eruptions and can be associated with large uncertainties (e.g. average or maximum
48 plume height, cumulative erupted volume, mass flow rate, grain-size distribution), and,
49 therefore, do not contribute significantly to our comprehension of the volcanic system. This
50 is particularly true for prehistoric eruptions that occurred when no observations of the
51 plume and of the meteorological conditions could be made. Due to the complex dynamics
52 that characterize many eruptive events, the derivation and interpretation of these
53 parameters is not always straightforward even for recent, directly observed eruptions and
54 many strategies can be applied that are associated with various degrees of uncertainty.
55 Tephra deposits associated with long-lasting eruptions can be further complicated by the
56 combination of varying eruptive and atmospheric conditions in time.

57

58 Here we discuss the case of the 2011 rhyolitic eruption of Cordón Caulle volcano
59 (Chile) that caused widespread disruption to various economic sectors and human

60 activities, representing a complex eruptive event that needs to be described in detail in
61 order to characterize the range of the associated time-dependent Eruption Source
62 Parameters (ESPs) and mitigate future risks. Only a few rhyolitic eruptions have been
63 studied in detail (e.g., Chaitén 2008 eruption, Chile; [Alfano *et al.*, 2011; Castro and
64 *Dingwell*, 2009; *Folch et al.*, 2008]). They are characterized by an initial climactic phase
65 associated with both convective plumes and Pyroclastic Density Currents (PDCs) followed
66 by lava effusion, and month-long low-intensity, ash-laden plumes [Castro *et al.*, 2013]. The
67 2011 eruption of Cordón Caulle volcano also provides the unique opportunity to explore i)
68 the interaction between plume dynamics and atmospheric wind and ii) the complex
69 interplay amongst cloud gravitational spreading, atmospheric diffusion and wind advection
70 of small-moderate eruptions, which have recently been topics of lively debates within the
71 international community [e.g., *Carazzo et al.*, 2014; *Costa et al.*, 2013; *Degruyter and*
72 *Bonadonna*, 2012; 2013; *Devenish*, 2013; *Mastin et al.*, 2014; *Woodhouse et al.*, 2013]. A
73 detailed characterization of the stratigraphy and deposit features is presented by *Pistolesi*
74 *et al.* [2015], while specific aspects of tephra sedimentation and grain-size are presented
75 by *Bonadonna et al.* [2015]. Here we focus on the determination of key physical parameters
76 of the main eruptive phases in relation to eruption classification (i.e. erupted mass, plume
77 height, mass flow rate and eruption duration) and on the characterization of plume
78 dynamics and cloud spreading.

79

80 **2. Eruption chronology**

81 Cordón Caulle, part of the Puyehue-Cordón Caulle volcanic complex located in the Central
82 Andes, produced large rhyodacitic fissure eruptions of Volcanic Explosivity Index (VEI) 3 in
83 1921–1922 and 1960, whereas two VEI 5 eruptions had occurred about 860 BP and 5000

84 BC but were associated with the Puyehue stratovolcano (GVP, Global Volcanism Program,
85 <http://www.volcano.si.edu>; [Siebert *et al.*, 2010]). After about 41 years of repose, an
86 eruption started at Cordón Caulle volcano on June 4, 2011, around 18:30 UTC according to
87 Geostationary Operational Environmental Satellite (GOES) images. The climactic phase
88 (~27 hours; [Jay *et al.*, 2014]) was associated with a ~9-12 km-high plume (above vent, with
89 a vent height of about 1.5 km) that dispersed most of the tephra towards E and SE (Fig. 1)
90 [Castro *et al.*, 2013; Collini *et al.*, 2013; Pistolesi *et al.*, 2015].

91 The tephra deposit associated with the first week of the eruption (June 4-11, 2011)
92 was studied based on about 70 outcrops located between 1 and 240 km from the active
93 vent and was subdivided into three main units: Unit I, layers A to F; Unit II, layers G to H;
94 and Unit III, layers K1 to K5 (see Pistolesi *et al.* [2015] for more details on the field surveys
95 and Bonadonna *et al.* [2015] and Supporting Information for isomass maps of individual
96 phases). In particular, Unit I was mostly deposited towards SE (June 4-5, 2011), Unit II
97 towards the N (June 5-6, 2011) and Unit III towards the E (June 7-11, 2011). Up-wind
98 sedimentation was negligible during all phases. PDCs were generated on June 4, 5 (with a
99 runout of ~10 km; [SERNAGEOMIN/OVDAS, 2011] Servicio Nacional de Geología y
100 Minería/Observatorio volcanológico de los Andes del Sur), 8 and 14, whereas, on June 10,
101 destructive lahars were triggered by heavy rains. Onset of lava effusion was reported on
102 June 15. Lava was still moving at a low rate by April 2012 [Tuffen *et al.*, 2013].

103

104 **3. Physical parameters and eruption classification**

105 **3.1 Plume height and wind speed**

106 A population of 20 lithic clasts was collected at selected outcrops; three orthogonal axes of
107 each clast (with the approximation of the minimum ellipsoid) were measured and the

108 associated geometric mean (i.e. the cube root of the product of the three axes) of the 50th
109 percentile and of the 5 largest clasts were determined in order to compile two isopleth
110 maps and validate the representativeness of largest-clast values [Bonadonna et al., 2013]
111 (Fig. 2). Selected samples were also collected for grain-size distribution. The map of median
112 diameter $Md\phi$ [Inmann, 1952] of the cumulative Unit I (layers A-F) is shown in Fig. 3, while
113 detailed grainsize analyses are reported in Bonadonna et al. [2015].

114 The two isopleth maps of Fig. 2 were used to determine the maximum plume height
115 for Unit I (cumulative layers A-F) applying the method of Carey and Sparks [1986]. As
116 described in Bonadonna et al. [2013], the isopleth map based on the 50th percentile is
117 expected to be more representative of the grain-size variation around the volcano, but being
118 associated with lower grain-size values than the map based on the 5 largest clasts, it is
119 typically associated with lower plume heights (e.g. Biass and Bonadonna [2012]).
120 Nonetheless, the two isopleth maps shown in Fig. 2 are very similar, with the 0.8 and 1.6 cm
121 being slightly more elongated for the geometric mean of the 5 largest lithic clasts with respect
122 to the 50th percentile. For both maps we obtained a maximum plume height of about 18 ± 3
123 km and 15 ± 3 km above sampling height (a.s.h.), i.e. mean elevation of the isopleth contours
124 (~ 930 m above sea level, a.s.l.), for the 0.8 cm and the 1.6 cm contours, respectively (the error
125 is based on the assumption of an intrinsic 20% error for this method; Carey and Sparks
126 [1986]). A maximum wind at the tropopause of about 40 m s^{-1} was also determined for both
127 contours and both maps. The plume height of A-F was also calculated based on the Weibull
128 fit of both largest lithics (LL) and $Md\phi$ [Bonadonna and Costa, 2013a] (Figs. 2a and 3). Both
129 isopleth maps for the lithics resulted in a plume height of about 13 ± 3 km a.s.h., while the $Md\phi$
130 map resulted in a plume height of about 10 ± 2 km a.s.h. (still assuming a 20% intrinsic error
131 associated with the method; Bonadonna and Costa [2013]) (Table 1). It is important to

132 highlight that plume heights derived based on the method of *Carey and Sparks* [1986] and of
133 *Bonadonna and Costa* [2013] (LL strategy) are maximum (peak) values, whereas the plume
134 height from *Bonadonna and Costa* [2013] (Md ϕ strategy) are average values. This is related
135 to the fact that the LL strategies capture the most intense stage of the associated eruptive
136 phase, while the Md ϕ strategy describes the whole deposit and tends to average the
137 fluctuation of eruptive conditions. In addition, the method of *Carey and Sparks* [1986] is based
138 on plume vertical velocity for strong plumes and only accounts for the effect of wind at the
139 spreading height, while the Cordón Caulle plume was probably characterized by lower plume
140 ascent velocity and was clearly affected by wind advection along the whole rise height (see
141 section 3.3). This results in an overestimation of plume height.

142

143 3.2 Erupted mass

144 The volume of individual phases, derived by *Pistolesi et al.* [2015] based on three empirical
145 strategies (i.e. exponential, power-law and Weibull fits), was converted into erupted mass
146 based on the average measured deposit density (i.e. 560 kg m⁻³ for A-F and 600 kg m⁻³ for H
147 and K2, *Bonadonna et al.* [2015]). Values of $1.2 \pm 0.06 \times 10^{11}$, $4.2 \pm 0.9 \times 10^{11}$, $1.3 \pm 0.4 \times 10^{11}$ and
148 $2.8 \pm 0.7 \times 10^{10}$ kg were obtained for A-B, A-F, H and K2 layers, respectively, resulting in a total
149 mass of $5.7 \pm 1.0 \times 10^{11}$ kg (i.e., A-F+H+K2) (mean and standard deviation are calculated based
150 on the different empirical strategies used).

151 Erupted mass was also calculated for layers A-B and A-F based on the inversion of the
152 advection-diffusion model TEPHRA2 [*Bonadonna et al.*, 2005b] according to the downhill
153 simplex strategy developed by *Connor and Connor* [2006] to find the best set of eruptive
154 parameters through the comparison between observed and computed mass accumulation
155 per unit area. The deposits of H and K2 were not inverted due to the relatively large fraction

156 of fine ash that cannot be easily reproduced by TEPHRA2 without describing particle
157 aggregation. A systematic search of minimum values of the Root Mean Square Error (RMSE)
158 was carried out to assess the presence of multiple minima (Fig. 4) before performing targeted
159 inversions. The whole range of eruptive parameters explored include erupted mass, plume
160 height and grain-size features (i.e., M_{dphi} and sorting). RMSE is a good measure of accuracy
161 but it is scale-dependent and, therefore, it is only good to compare goodness of fit within each
162 analysis. Due to model sensitivity and interaction with other input parameters, the erupted
163 mass is typically better constrained than plume height (e.g. [Bonadonna and Costa, 2013b;
164 Scollo et al., 2008]). In fact, if only the coarse fraction of A-F layer is inverted (-5 to 3 ϕ), a
165 better constraint is obtained for plume height, which is in agreement with observations (Fig.
166 4c); however, the associated mass is related only to the coarse fraction (i.e. ~85% of total
167 mass; Bonadonna et al. [2015]). Nonetheless, also the erupted mass for both layers A-B and
168 A-F is not as well constrained by the model as for larger eruptions (e.g. Pululagua 2450BP
169 [Volentik et al., 2010]; 4-ka Rungwe Pumice [Fontijn et al., 2011]), with many relative RMSE
170 minima associated with both an underestimation and an overestimation of the erupted mass
171 as derived from empirical integrations (dashed lines in Fig. 4). Targeted inversions were run
172 based on the ranges identified by both the minimum values of RMSE shown by Fig. 4 and
173 empirical observations (see Supporting Information for more details). The best fit of erupted
174 mass for the whole deposit was found for values of 2.8×10^{11} kg, 5.4×10^{11} kg and 2.0×10^{11} kg
175 for A-B, A-F and the coarse fraction of A-F, respectively, which are in good agreement with
176 the mass calculated from mapped deposit based on empirical strategies. Associated plume
177 heights are 13.0, 13.5 and 13.1 km a.s.l. also in agreement with observations (Supporting
178 Information and Table 1). Averaging results of empirical and analytical methods, we conclude

179 that the erupted mass associated with A-B and A-F are $1.6\pm 0.8 \times 10^{11}$ and $4.5\pm 1.0 \times 10^{11}$,
180 respectively. Total mass for A-F+H+K2 becomes $6.0\pm 1.1 \times 10^{11}$ kg.

181

182 3.3 Mass Flow Rate

183 A detailed account of observed plume heights during the whole eruption was compiled by
184 both *Collini et al.* [2013] and the GVP as provided by the Buenos Aires Volcanic Ash Advisory
185 Center and SERNAGEOMIN (03/2012 (BGVN 37:03);
186 http://www.volcano.si.edu/volcano.cfm?vn=357150#bgvn_3703; Fig. 5, Table 1 and
187 Supporting Information). The interaction between plume rise and wind advection is well
188 shown by the Aqua satellite image that captured the first development of the volcanic cloud
189 on June 4 while it was passing over Villa La Angostura (about 40 km from the Chilean border)
190 and by the Futangue stationary camera images between June 13 and 20, 2011 (Fig. 5). All
191 images show negligible up-wind spreading, with a small inclination of the rising plume (based
192 on the Aqua satellite image). The Aqua satellite image also highlights the heterogeneity of the
193 volcanic cloud, with a distinct puff-like structure ($\sim 15 \times 17$ km) close to the vent, which is about
194 1.5 km higher than the main cloud (~ 10 km above ground; heights calculated based on cloud
195 shadow clinometry; e.g. *Holasek and Self* [1995]) (Supporting Information). Such a feature
196 suggests a pulsating dynamics typical of long-lasting plumes (e.g. Eyjafjallajökull 2010 plume;
197 e.g. *Ripepe et al.* [2013]).

198 MFR between June 4-30, 2011 was calculated between $\sim 10^4$ and $\sim 10^7$ kg s^{-1} using the
199 method of *Degruyter and Bonadonna* [2012] that accounts for the effects of wind advection
200 and thermal stratification of the atmosphere on the plume height (Fig. 6a):

201

$$MFR = \pi \frac{\rho_{a0}}{g'} \left(\frac{\alpha^2 \bar{N}^3}{10.9} H^4 + \frac{\beta^2 \bar{N}^2 \bar{v}}{6} H^3 \right) = \pi \frac{\rho_{a0}}{g'} \frac{\alpha^2 \bar{N}^3}{10.9} H^4 \left(1 + \frac{1}{\Pi} \right) \quad (1)$$

203

204 where H is plume height above the vent (m), \bar{N} is the average buoyancy frequency (s^{-1}) across
 205 the plume height and quantifies the thermal stratification of the atmosphere, \bar{v} is the
 206 average wind velocity across the plume height ($m s^{-1}$), α is the radial entrainment coefficient,
 207 β is the wind entrainment coefficient, ρ_{a0} is the atmospheric density at the vent ($kg m^{-3}$) and
 208 g' ($m s^{-2}$) is equivalent to the reduced gravity based on the difference in sensible heat between
 209 the gas-pyroclast mixture and the ambient sensible heat at the source (i.e.,

$$210 \quad g' = g \left(\frac{c_0 \theta_0 - c_{a0} \theta_{a0}}{c_{a0} \theta_{a0}} \right), \text{ where } c_0, \theta_0, c_{a0} \text{ and } \theta_{a0} \text{ are the eruption heat capacity, eruption}$$

211 temperature, reference heat capacity and reference temperature, respectively). The quantity

212 Π is a scaling parameter and is defined below (eq. 2). For the plume height we use the

213 minimum and maximum value reported from all sources mentioned above (Supporting

214 Information). We use the wind, humidity, temperature and pressure data provided by

215 ECMWF (European Centre for Medium-Range Weather Forecasts) ERA-Interim at a 0.25°

216 resolution [Dee *et al.*, 2011] and calculate the average wind speed across the plume height

217 using trapezoidal integration (Fig. 5 and Supporting Information). From these we calculate the

218 average buoyancy frequency across the plume height and the density of the atmosphere at

219 the vent height. For the specific heat capacity of air we use $998 J kg^{-1} K^{-1}$ [Woods, 1988]. The

220 specific heat capacity and the temperature of the gas-pyroclast mixture at the vent and both

221 the radial and wind entrainment coefficients are uncertain and we therefore use a range of

222 values. Common eruption temperatures for silica-rich eruptions are between 1118 and 1216

223 K [Castro *et al.*, 2013; Jay *et al.*, 2014]. The specific heat capacity of the gas-pyroclast mixture

224 is dependent on the eruption temperature. We use the parameterization of *Dufek et al.*
225 [2007] and of *Whittington et al.* [2009] and find a range between 1197 and 1211 J kg⁻¹ K⁻¹ for
226 the explored temperature range. For the radial entrainment coefficient we use values
227 between 0.05 and 0.15 [e.g., *Carazzo et al.*, 2008; *Morton et al.*, 1956; *Suzuki and Koyaguchi*,
228 2010] and for the wind entrainment coefficient we use values between 0.1 and 1 [e.g., *Briggs*,
229 1972; *Bursik*, 2001; *Contini et al.*, 2011; *Degruyter and Bonadonna*, 2012; *Devenish*, 2013;
230 *Devenish et al.*, 2010; *Hewett et al.*, 1971; *Huq and Stewart*, 1996; *Mastin*, 2014; *Suzuki and*
231 *Koyaguchi*, 2013], respectively.

232 The uncertainty within the observations (i.e. plume height and atmospheric data) do
233 not allow for an accurate estimate of the MFR. Uncertainty is further increased by the
234 uncertainty within model parameters (i.e. entrainment coefficients and eruption source
235 temperature). We demonstrate the large errors that can arise in MFR from the combination
236 of these uncertainties in Fig. 6 (see also Fig. S4 in Supporting Information for a comparison
237 with traditional strategies not accounting for wind entrainment). The uncertainty associated
238 with the height and atmospheric observations (indicated by the blue bars in Fig. 6) induces an
239 uncertainty of an order of magnitude to several orders of magnitude. The additional
240 uncertainty that stems from the model parameters increase the uncertainty further by several
241 orders of magnitude (indicated by the white bars in Fig. 6). In spite of the large uncertainty,
242 we can compare the relative values of the MFR estimates. To this end we use the log average
243 value of the minimum and maximum MFR calculated for the observational uncertainty, i.e.
244 the blue bars.

245 Two main eruptive periods can be distinguished based on MFR values: the first period
246 with largely fluctuating MFR >10⁶ kg s⁻¹ (between June 4-14; Unit I, II and III) and the second
247 period with MFR <10⁶ kg s⁻¹ (after June 14). The highest average MFR was estimated for the

248 climactic phase (i.e. June 4; layers A-B), i.e. $0.9 \times 10^7 \text{ kg s}^{-1}$ (Table 1). This is in agreement with
 249 the GVP reports on the eruption, based on the daily bulletins of OVDAS, which describe that
 250 eruption started to decrease in intensity by the end of the first day, and with the observed
 251 features of the deposits [Pistolesi et al., 2015]. The influence of wind entrainment on plume
 252 rise was strong throughout the whole eruption, as shown by the distortion of the volcanic
 253 clouds towards the wind direction with no obvious up-wind spreading (Fig. 5). The wind effect
 254 on plume rise can be quantified by the ratio of the radial-entrainment and the wind-
 255 entrainment terms in eq. (1) or, in other words, the ratio of the characteristic timescale for
 256 wind entrainment and the characteristic time-scale for plume rise in a wind-still environment:

$$258 \quad \Pi = \frac{\overline{NH}}{1.8\overline{v}} \left(\frac{\alpha}{\beta} \right)^2 \quad (2)$$

259

260 *Degruyter and Bonadonna* [2012] suggested that Π can be used to distinguish between strong
 261 ($\Pi \gg 1$) and weak plumes ($\Pi \ll 1$). This has recently been confirmed by laboratory experiments
 262 [G Carazzo et al., 2014]. We define here weak and strong plumes by $\Pi < 0.1$ and $\Pi > 10$,
 263 respectively; plumes characterized by $0.1 < \Pi < 10$ are transitional between strong and weak
 264 (Fig. 7a). *Carazzo et al.* [2014] defined this category as distorted plumes. It is important to
 265 stress that the boundary values of 0.01 and 10 for the classification of weak and strong
 266 plumes, respectively, are to be considered as indications for comparative analysis more than
 267 absolute values, as they strongly depend on the choice of entrainment coefficients. In fact,
 268 similar to the MFR, the value of Π can suffer from large uncertainties (e.g., Fig. 7b). The
 269 difference here is that the observational uncertainty from height and atmospheric data is
 270 quite small and allows estimating Π within an order of magnitude or less. The additional

271 uncertainty within the entrainment coefficients, however, creates a very large uncertainty of
 272 several orders of magnitude. As in the case of the MFR, we use the log average value of the
 273 minimum and maximum MFR calculated for the observational uncertainty, i.e. the blue bars,
 274 to relatively compare differences in the influence of wind.

275 Throughout the whole eruption the characteristic time for wind entrainment is faster
 276 than the timescale for rise in a wind-still environment, i.e. $\Pi < 1$, and thus the contribution of
 277 wind is significant. In particular, Π fluctuates between 0.02 and 0.17 (black circles in Fig. 7b)
 278 and does not correlate with MFR. In fact, while MFR quantifies the eruption intensity,
 279 Π quantifies the plume interaction with the atmosphere. This is most prominently
 280 demonstrated by the periods of June 4-6 and June 20-22 that are both associated with
 281 transitional plumes (i.e., $0.1 < \Pi < 10$) indicating that wind is significant but not dominating the
 282 plume rise height (Figs 5c and d, 7). However, these periods can be distinguished by a high
 283 intensity ($\text{MFR} > 10^6 \text{ kg s}^{-1}$) for the first period, but a low intensity ($\text{MFR} < 10^6 \text{ kg s}^{-1}$) for the latter
 284 period. The periods of June 7-12, 14-19 and 23-30 were characterized by weak plumes
 285 ($\Pi < 0.1$), for which wind is the controlling factor of the plume height (Figs 5 and 7). They were
 286 also of varying intensity (Fig. 7). To give additional insight into the meaning of Π , we use it to
 287 estimate how much the effective height of the plume is reduced compared to the height the
 288 plume would have reached if rising in a wind still environment (term H_{nowind}). Using eq. 1
 289 we find that:

$$291 \quad \frac{H}{H_{\text{nowind}}} = \left(\frac{1}{1 + \left(\frac{1}{\Pi} \right)} \right)^{\frac{1}{4}} \quad (3)$$

292

293 For the days with highest Π (i.e. 0.1-0.2; i.e. June 4-6 and 20-22) the actual plume height is
294 between 55% and 64% of the height it would have been under wind-still conditions, while the
295 days with lowest Π (i.e. 0.02-0.05) this would range between 37% and 47%.

296

297 3.4 Eruption duration

298 Based on the evaluation of the average MFR with time (Fig. 6) and the estimated erupted
299 mass for each phase as reported in Table 1, an approximate duration of each phase was
300 determined and compared with data derived from direct observation. In particular, A-B, A-
301 F, H and K2 layers resulted to be associated with a mean duration of 5.1, 17.2, 8.3 and 3.2
302 hours, respectively (Table 1). Durations of the sustained phases are likely to be longer if we
303 consider the estimated erupted mass as minimum values due to the intrinsic uncertainty
304 associated with the volume calculations based on both empirical fitting and analytical
305 inversion [Bonadonna and Costa, 2012] and the calculated MFR as associated to maximum
306 values of plume height as reported by both Collini *et al.* [2013] and GVP (Table 1). In
307 addition, the determination of plume height can be associated with significant
308 uncertainties even for recent eruptions [Oddsson *et al.*, 2012; Prejean and Brodsky, 2011;
309 Tupper and Wunderman, 2009]. Considering the 4th power relation between MFR and
310 plume height (eq. 1), even small uncertainties in plume height measurements could result
311 in large MFR uncertainties, and, therefore, duration uncertainties. The uncertainty in MFR
312 from both plume-height observations and atmospheric conditions (blue bars in Fig. 6) for
313 the June 4-6 (20-30%) and June 7 (50%) events results in an even larger duration
314 uncertainty, i.e. 85-95% (Table 1 and Supporting Information). Additional sources of
315 uncertainty stem from the model assumptions, such as entrainment coefficients and
316 eruption temperature (white bars in Fig. 6). However, considering the good agreement

317 between eruption duration derived from MFR analysis and duration of the various eruption
318 phases as observed from satellite images (i.e. 24-30 hours for A-F and <12 hours for H and
319 K2; [Pistolesi et al., 2015]), we suggest that both eruptive and atmospheric conditions did
320 not vary significantly within each of the studied phases.

321

322 3.5 Eruption classification

323 Given the complexity of characterizing and classifying long-lasting eruptions, here we
324 consider both individual and cumulative phases and discuss the resulting implications. The
325 phase A-F of the Cordón Caulle eruption could be classified based on erupted volume/mass,
326 MFR, plume height, thickness, LL and $Md\phi$ data. In particular, a total volume/mass of
327 $0.80\pm 0.17 \text{ km}^3/4.5\pm 1.0\times 10^{11} \text{ kg}$ results in a VEI 4 [Newhall and Self, 1982] and a magnitude of
328 4.6 [Pyle, 2000] (Table 1). Based on the MFR versus plume height classification of Bonadonna
329 and Costa [2013], only the plume developed on June 4 can be classified as subplinian, whereas
330 all other plumes plot in the field of small-moderate eruptions (Fig. 8). The classification plot
331 based on Weibull thickness and LL parameters for the A-F layers results in small-moderate
332 eruptions transitional to subplinian, whereas Weibull parameters of thickness versus $Md\phi$
333 result in clear small-moderate eruptions [Bonadonna and Costa, 2013a] (Fig. 9). Finally, given
334 that the thinning trend of A-F layers can be described by 3 exponential segments on a
335 $\log(\text{thickness})$ versus square root of area [Pistolesi et al., 2015], three values of b_t can be
336 obtained (i.e. 2.9, 8.3 and 24.4 km) and, therefore, three values of ratio b_c/b_t (i.e. 2.8, 1.0 and
337 0.3 for the isopleth map of Fig. 2a), with b_t and b_c being the distance over which the maximum
338 thickness and the size of the largest clast decrease by half, respectively [Pyle, 1989]. These
339 parameters plot in the field of plinian to ultraplinian eruptions in the classification scheme of
340 Pyle [1989]. Given the available dataset, the phases A-B ($0.28\pm 0.15 \text{ km}^3$), H ($0.21\pm 0.07 \text{ km}^3$)

341 and K2 ($0.05 \pm 0.01 \text{ km}^3$) could only be classified based on erupted volume and mass and can
342 be associated with VEI 4 (A-B and H) and 3 (K2) and magnitude 4.2 (A-B), 4.1 (H) and 3.4 (K2),
343 respectively (Table 1).

344

345 **4. Cloud spreading**

346 When they reach the level of neutral buoyancy, vigorous plumes start spreading as gravity
347 currents as they are denser at their top and less dense at their base than the surrounding
348 stratified atmosphere, and their crosswind spreading is proportional to the volumetric flow
349 rate at the neutral buoyancy level [e.g. *Sparks et al.*, 1997]. As a result, higher plumes would
350 spread laterally more rapidly than lower plumes such that [*Bonadonna and Phillips*, 2003]:

351

$$352 \quad w = \frac{2x}{1 + a\sqrt{x}} \quad (4)$$

353

354 with $a = \frac{u}{\sqrt{\lambda N Q / \varepsilon}}$, where w is the crosswind width (m), x is the downwind distance (m),

355 u is the wind velocity at the neutral buoyancy level (m s^{-1}), Q is the volumetric flow rate at
356 the neutral buoyancy level ($\text{m}^3 \text{ s}^{-1}$), which we determined with the 1D model of *Degruyter and*
357 *Bonadonna* [2012] (Supporting Information), N is the atmospheric buoyancy frequency (s^{-1})
358 assumed to be 0.01 s^{-1} for these calculations as all plumes developed in the troposphere, λ is
359 a constant of the order of unity that depends on flow geometry and ambient stratification
360 (here 0.8), and ε is a geometrical perimeter factor assumed to be 3.9 (with an uncertainty on
361 the calculated cloud width of 25%; see *Bonadonna and Phillips* [2003] for more details). In
362 contrast, plumes that are strongly affected by wind maintain the vorticity structure

363 characteristic of the convective column also when they reach their maximum height and start
364 spreading horizontally [*Sparks et al.*, 1997]. Their crosswind spreading at the neutral
365 buoyancy level is typically described by turbulent diffusion (i.e. Fickian diffusion) such that
366 [*Bursik*, 1998]:

367

$$368 \quad w = 4 \sqrt{\frac{Kx}{u}} \quad (5)$$

369

370 where K is the horizontal eddy diffusivity, i.e. diffusion coefficient ($\text{m}^2 \text{s}^{-1}$). We have
371 already shown how the plumes developed on June 4 and 6 were transitional between weak
372 and strong plumes. Downwind (distance from vent) and crosswind (width) distances and
373 velocities were calculated from GOES images for the cloud developed on both days in order
374 to establish the relative contribution of gravitational spreading (Fig. 10). A significant wind
375 shift is evident on June 6, with the cloud first spreading towards NE and then moving SE
376 and towards the Atlantic Ocean. Due to the constraint of satellite images, the spreading of
377 the SE cloud of June 6 could not be analyzed. Width and downwind length of the isomass
378 maps of the A-F deposit (i.e. Unit I – June 4-5; Supporting Information) were also
379 investigated and compared with the cloud geometry.

380 The best fit is given by the linear combination of gravity spreading and turbulent
381 diffusion following *Bursik* [1998] with a diffusion coefficient of $9,000 \text{ m}^2 \text{ s}^{-1}$ for both days
382 (Fig. 11a). The observed crosswind width lays in between the linear combination of
383 gravitational spreading and turbulent diffusion for the minimum and maximum
384 observations of volumetric flow rate (solid and dashed lines, Fig. 11a). The range of
385 volumetric flow rate depends on the uncertainty on both plume height and atmospheric

386 conditions (see Fig. 5e). Radial entrainment, wind entrainment and eruption temperature
387 were fixed to 0.1, 0.5 and 1167 K, respectively. The dispersal of the 1 kg m⁻² isoline of Unit
388 I (deposited on June 4-5) can also be described by the linear combination of gravity
389 spreading and turbulent diffusion (Fig. 11a). Relative contribution of the gravitational
390 spreading is 49-71% and 40-50% for minimum and maximum volumetric flow rate of June
391 4 and 6, respectively, with no significant variation with distance from vent (standard
392 deviation <2%). Results for eq. 5 (Fickian diffusion; Fig. 11b) and eq. 4 (gravitational
393 spreading; Fig. 11c) have also been plotted separately. Fickian diffusion seems to be able
394 to describe the cloud spreading of both June 4 and June 6, but only if unrealistic values of
395 diffusion coefficients are considered (i.e., 90,000 and 30,000 m² s⁻¹, respectively), which are
396 higher than the range expected for atmospheric dispersion over brief time intervals (10-
397 10⁴ m² s⁻¹; [Heffter, 1965; Pasquill, 1974]). Finally, pure gravitational spreading seems to
398 underestimate the observed cloud spreading for both days, with the largest discrepancies
399 being associated with the June 6 event (Fig. 11c).

400 The downwind and crosswind velocity of the cloud were calculated based on the
401 distance from vent and from the central axis, respectively, as observed from GOES images
402 of Fig. 10 and the associated observation times (Fig. 12). The downwind velocity is higher
403 than the associated wind velocity at the neutral buoyancy level and such a discrepancy is
404 due to the contribution of the gravitational component to plume spreading. The velocity
405 due to gravitational spreading, u_b , was calculated with the equation of *Bonadonna and*
406 *Phillips* [2003]:

$$408 \quad u_b = \sqrt{\frac{\lambda N Q}{\epsilon x}} \quad (6)$$

409

410 which is equivalent to eq. 10 of *Costa et al.* [2013]. Our results show that for both plumes
411 considered (i.e. June 4 and June 6), the crosswind velocity can be well described by a lateral
412 spreading due to buoyancy, while the downwind velocity can be described by a linear
413 combination of wind advection and gravitational spreading (Fig. 12). In particular, the
414 crosswind velocity of June 4 is between 6 and 10 m s⁻¹, while the crosswind velocity of the
415 NE cloud of June 6 is between 1 and 2 m s⁻¹. As a comparison, the crosswind velocity of the
416 SE cloud of June 6 is between 0 and 1 m s⁻¹. Downwind velocity of June 4 and 6 (NE cloud)
417 is between 35-45 m s⁻¹ and 17-21 m s⁻¹, respectively. Relative errors between observed and
418 calculated downwind velocity are <7% for June 4 and <13% for June 6. The distal increase
419 in downwind velocity for both June 4 and June 6 seem to be mostly related to a local
420 increase in wind velocity.

421

422 **5. Discussion**

423 The 2011 eruption of Cordón Caulle, together with the 2008-2009 eruption of Chaitén
424 (Chile), represent rare cases of rhyolitic eruptions that have been witnessed and studied in
425 detail. They were both long-lasting and caused widespread disruption to various economic
426 sectors and transport systems, mostly in Argentina due to the prevailing westerly winds
427 that characterize the middle latitudes. The associated large amount of airborne ash caused
428 major disturbance to aviation in Argentina, and, to a lesser extent, in Australia and New
429 Zealand that, however, was not as severe as in Europe during the 2010 Eyjafjallajökull
430 eruption only due to less dense air traffic [e.g. *Collini et al.*, 2013; *Folch et al.*, 2008]. In
431 addition, *Castro and Dingwell* [2009] showed how, regardless of the high silica content,
432 rhyolitic eruptions can develop quickly most likely because they are associated with shallow

433 magma chambers [Wicks *et al.*, 2011] that often exist at near-liquidus, hydrous magmatic
434 conditions. Consequently, rhyolitic magmas may have lower viscosities than expected
435 [Castro *et al.*, 2013; Jay *et al.*, 2014] and are, therefore, highly mobile. As a result, a detailed
436 account of physical parameters, such as erupted mass, MFR, plume height, eruption
437 duration constrained in this study (Table 1) in combination with total grain-size distribution
438 [Bonadonna *et al.*, 2015], and their variation with time is particularly important to forecast
439 future eruptions and mitigate the associated risk. In addition, the eruptive dynamics of
440 long-lasting small-moderate eruptions, such as that of Cordón Caulle, is complicated by the
441 interaction with the variable atmospheric and source conditions, which make the
442 characterization of the physical parameters and the classification of the eruption more
443 challenging than for short powerful eruptive events.

444

445 *Eruption classification*

446 Due to its long-lasting character and the variation of eruptive parameters through time, the
447 2011 Cordón Caulle eruption represents a typical example of an eruption that can be
448 classified with different eruptive styles depending on the strategy used and the section of
449 the deposit considered. The MFR versus height plot suggested by Bonadonna and Costa
450 [2013] shows the transitional character from subplinian to small-moderate eruptions for
451 the different eruptive phases, also confirmed by the Weibull parameters fitting the LL and
452 $Md\phi$ trends. The classification of small-moderate eruptions based on the $Md\phi$ plot (Fig. 9),
453 as opposed to transitional between small-moderate and subplinian, can be explained with
454 $Md\phi$ values being slightly underestimated due to breakage of the most abundant variable-
455 density juvenile clasts, and the constant presence of a fine-grained subpopulation which
456 tends to decrease the $Md\phi$ value [Bonadonna *et al.*, 2015]. Conversely, the use of the

457 exponential parameters b_t and b_c/b_t of *Pyle* [1989] is made complex by the presence of
458 multiple segments in the log(thickness) vs. square root of isopach area diagram of layers A-
459 F and, therefore, multiple values.

460 Finally, it is important to discuss the application of the VEI and Magnitude scale to
461 long-lasting eruptions with different eruptive styles [e.g. Siebert et al. 2010]. VEI and
462 Magnitude values vary depending on the eruptive phases considered in the calculation. If
463 individual phases/layers are considered, VEI and Magnitude values range between 3 (K2) -
464 4 (H) and 3.4 (K2) - 4.1 (H), respectively. However, if the cumulative tephra deposits of A-F
465 or A-F+H+K2 are considered (i.e., June 4 and the period between June 4-15, 2011,
466 respectively), a VEI 4-5 and Magnitude 4.6-4.8 are obtained, respectively. It is clear in this
467 case that any correlation between VEI and eruption intensity (i.e., column height) implicit
468 in the VEI formulation is not correct. Unfortunately, individual layers A to F could not be
469 distinguished through the whole deposit and, therefore, associated volume could not be
470 calculated. It is often the case that individual layers of long-lasting eruptions cannot be
471 easily distinguished in the field and the volume of cumulative deposits represents the only
472 available information. One should also bear in mind that VEI and Magnitude values of
473 cumulative deposits of short- and long-lasting eruptions cannot be directly compared,
474 above all when durations are significantly different (e.g. a few hours versus a few
475 days/weeks/months). It is also important to consider that the VEI values calculated for
476 Cordón Caulle do not include the volume of associated PDCs, even though in the original
477 interpretation by *Newhall and Self* [1982], VEI should be based on the total volume of ejecta
478 (i.e. both tephra and PDC material).

479

480 *Mass Flow Rate, erupted mass and eruption duration*

481 The importance of the wind entrainment on the calculation of the MFR is shown in Fig. 6, with
482 discrepancies with traditional strategies up to one order of magnitude (see also Fig. S4 of
483 Supporting Information). Our results also show that, due to the interaction with variable
484 atmospheric conditions, plumes with similar height could be associated with different MFR
485 values. As an example, plumes developed on June 27-30 have similar heights, or even lower,
486 than the plumes developed on June 22-26, but are characterized by higher MFR values (i.e.
487 $3.0\text{-}4.6 \times 10^5 \text{ kg s}^{-1}$ and $0.2\text{-}3.4 \times 10^5 \text{ kg s}^{-1}$, respectively; Fig. 5e and 6). *Collini et al.* [2013] also
488 accounted for the effects of wind on plume rise but, for the period June 4-19, 2011, obtained
489 lower values of average MFR (i.e. $1.7 \times 10^6 \text{ kg s}^{-1}$), and higher values of erupted mass (i.e.
490 $2.4 \times 10^{12} \text{ kg}$). These values are nearly half of the average MFR derived from the analytical
491 equation of *Degruyter and Bonadonna* [2012] for the June 4-19 period, i.e. $3.3 \times 10^6 \text{ kg s}^{-1}$, due
492 to a different choice of plume-height values and model assumptions most likely related to the
493 radial and wind entrainment coefficients. However, the total erupted mass of *Collini et al.*
494 [2013] is larger than our values (i.e., $6.0 \pm 1.1 \times 10^{11} \text{ kg}$, as averaged between empirical
495 integration and inversion strategies) probably because the authors have assumed a daily
496 constant MFR throughout the whole eruption. These discrepancies show the complexity and
497 high uncertainty associated with the characterization of even recent and observed volcanic
498 eruptions, confirming the importance of combining detailed field studies with modeling
499 strategies.

500 It is important to mention the complex application of inversion strategies to both layer
501 A-B and A-F, which does not result in well constrained solutions even for the erupted mass
502 (Fig. 4). Such a complexity cannot be related to the presence of a large mass of fine ash (the
503 $\geq 3 \phi$ fraction being smaller than $\sim 15\%$ of the total deposit), but is most likely due to the strong
504 advection of the eruptive column and the combination of multiple thin layers indicative of a

505 long-lasting pulsating activity difficult to be captured by semi-analytical models such as
506 TEPHRA2. Only well targeted inversion runs provide results in agreement in observations. The
507 calculations of the erupted mass and MFR are in broad agreement with the observed duration
508 of ~27 hours of *Jay et al.* [2014] and 24-30 hours of *Pistolesi et al.* [2015] (i.e. duration
509 between 6-54 hours; Table 1). Conversely, if the erupted mass associated with the first phase
510 (Unit I) is divided by the observed duration of ~27 hours, an average MFR of $4.6 \times 10^6 \text{ kg s}^{-1}$ is
511 found. This is in agreement with the average of the minimum MFR values calculated with the
512 analytical equation of *Degruyter and Bonadonna* [2012] for the first two days (i.e. $2.3 \times 10^6 \text{ kg}$
513 s^{-1}).

514

515 *Wind effect on plume dynamics*

516 Deposit features associated with the first phase of the eruption (Unit I) suggest
517 sedimentation from a plume strongly affected by wind advection. All maps describing the
518 tephra deposits are strongly elongated, i.e. isopleth maps of both LL and $Md\phi$ (Figs 2 and
519 3) and isomass maps of both total deposit and individual size categories (Supporting
520 Information and *Bonadonna et al.* [2015]). It is interesting to note how even the 1.6-cm
521 contour for both isopleth maps is elongated downwind (Fig. 2), indicating that both the
522 rising plume and the umbrella cloud were significantly affected by the wind, as also visible
523 from the satellite images (Fig. 5d). *Bursik et al.* [1992] and *Volentik et al.* [2010] have shown
524 how the 1.6-cm clasts are transitional between sedimentation from plume margins and
525 sedimentation from umbrella cloud for plume heights between 21 and 36 km (i.e. Fogo A
526 (Azores) and Pululagua 2450BP (Ecuador)). Considering the significantly lower plume of the
527 2011 Cordón Caulle eruption, we expect the 1.6-cm clasts to fall out before reaching the
528 neutral buoyancy level. In case of vertical plume, the 1.6-cm contour should have been

529 concentric around the vent, as shown by the isopleths of vigorous plumes (e.g. Fogo A
530 [*Walker and Croasdale, 1971*]; Novarupta 1912 [*Fierstein and Hildreth, 1992*]). In addition,
531 all isopleth contours suggest a wind speed at tropopause of $\sim 40 \text{ m s}^{-1}$ as derived with the
532 method of *Carey and Sparks [1986]*. However, ECMWF wind data show lower wind
533 velocities at the tropopause (i.e. $\sim 11 \text{ km}$ above sea level) than derived from the model of
534 *Carey and Sparks [1986]* for June 4-5 (i.e. $10\text{-}30 \text{ m s}^{-1}$) and very strong winds for the June
535 7-11 ($30\text{-}80 \text{ m s}^{-1}$) (Fig. 5). This is probably related to the fact that vertical velocity of Cordón
536 Caulle plumes are lower than typical Plinian plume velocity considered in the model of
537 *Carey and Sparks [1986]*, and caution is called in applying the model for the deposits of this
538 type of eruptions.

539 Our results demonstrate that plume height is not always a good indicator of
540 eruptive conditions at the vent as it is strongly controlled by the interaction with the
541 surrounding atmosphere. The scaling parameter Π incorporates these effects and can be
542 used to discriminate between strong, transitional and weak plumes (Fig.7). This parameter
543 is independent of the MFR as it is demonstrated by the occurrence of both transitional and
544 weak plumes in the high- and low-MFR period (Figs 5, 6 and 7). A careful analysis of the
545 influence of the wind on plume height has shown that wind is dominant in controlling the
546 rise height over the buoyancy by a factor of 6-46 throughout the whole month of June, and
547 by a factor of 6-8 during the first two days of the eruption (Unit I) (Π of 0.16-0.02 and 0.16-
548 0-13, respectively; Fig. 7b and Supporting Information). This is particularly clear in the
549 MODIS image of the first few hours of the eruption that show no-up-wind cloud spreading
550 (Fig. 5d), and in the GOES images of the following hours, showing a very limited up-wind
551 spreading with a stagnation point not farther than 5-10 km from the vent vertical (Fig. 10a).
552 Wind, thus, has an important first-order effect on the plume height and needs to be

553 accounted for when it is being used to invert for eruption source parameters. This effect
554 will be strongest for weak plumes, such as the ones produced during certain periods of the
555 2010 Eyjafjallajökull and the 2011 Cordón Caulle eruptions (minimum $\Pi = 0.02$ for both
556 eruptions; *Degruyter and Bonadonna, 2012*), but can also be significant for transitional
557 plumes. Examples of transitional plumes are those associated with certain periods of both
558 the 2010 Eyjafjallajökull and the 2011 Cordón Caulle eruptions (maximum $\Pi = 0.18$ and
559 0.17 , respectively; *Degruyter and Bonadonna, 2012*) and those of the Mount St. Helens
560 1980 eruption ($0.2 < \Pi < 0.34$; *Carazzo et al., 2014; Degruyter and Bonadonna, 2012*).

561 SERNAGEOMIN reported numerous PDCs at the beginning of the eruption (at least
562 five in the first two days), as well as at the onset of the (weaker) second eruptive period
563 (after June 14). Between the 6 and 13 of June much fewer PDCs were reported (e.g. GVP,
564 <http://www.volcano.si.edu>). Quantities involved in plume collapse, such as initial density
565 difference, vent radius, exit velocity, and overpressure will affect this behavior [*Valentine*
566 *and Wohletz, 1989*], but MFR calculations suggest fairly constant source conditions during
567 this period. The June 6-13 period is characterized by particularly strong winds (Fig. 5e),
568 which could increase the plume buoyancy due to entrainment of air by wind shear and limit
569 the formation of PDCs [*Degruyter and Bonadonna, 2013*].

570

571 *Cloud spreading*

572 Crosswind spreading of the clouds associated with the transitional plumes developed on 4
573 and 6 June could be best described by the linear combination of gravitational spreading and
574 turbulent diffusion with values of diffusion coefficients similar for both days (i.e. $9,000 \text{ m}^2 \text{ s}^{-1}$)
575 ¹), that are significantly higher than those observed for low-energy bent-over plumes
576 advected as lenses of aerosol and gas with nearly constant width (e.g., $\sim 10 \text{ m}^2 \text{ s}^{-1}$ for Mt

577 Augustine eruption, 3 April 1986; *Sparks et al.* [1997]; *Bursik* [1998] but are in the range of
578 observed horizontal diffusivity over brief time intervals ($10\text{-}10^4 \text{ m}^2 \text{ s}^{-1}$; [*Heffter*, 1965; *Pasquill*,
579 1974]). Contrary to the 1996 Ruapehu eruption for which the deposit was wider than the
580 cloud, both cloud spreading and deposit during the first couple of days of the Cordón Caulle
581 eruption seem to be characterized by similar crosswind dispersal (Fig. 11). In addition, the
582 Ruapehu clouds clearly spread at a similar velocity as the wind at the neutral buoyancy level
583 [*Bonadonna et al.*, 2005a], while the downwind velocity of the clouds developed during the
584 Cordón Caulle eruption can be better described by a linear combination of gravitational
585 spreading and wind advection. Discrepancies between calculated and observed values of
586 downwind velocity are <15%, which are mostly within the uncertainty related to geometry
587 assumptions (Fig. 12).

588 In order to distinguish between passive transport by wind and gravitational spreading,
589 *Costa et al.* [2013] defined the cloud Richardson number ($\text{Ri} \approx u_b^2/u^2$), whereby $\text{Ri} < 0.25$
590 indicates a cloud spreading dominated by wind advection and for $\text{Ri} > 1$ the transport is
591 density-driven. In the case of the Cordón Caulle eruption we find an average $\text{Ri} \sim 0.01\text{-}0.05$ on
592 June 4 and $\sim 0.003\text{-}0.01$ on June 6, which would suggest only passive transport plays a role.
593 However, our results suggest that the downwind velocity can be described by u_b+u (Fig. 12).
594 In this case, the fraction contributed by gravitational spreading is easily quantified by
595 $u_b/(u_b+u)$, which, in terms of Ri , becomes $1/(1+1/\sqrt{\text{Ri}})$. We find that the fraction of
596 gravitational spreading contributes between 8-19% and 5-9% of the total spreading for June
597 4 and 6, respectively. This suggests that gravitational spreading can be relevant for Ri down
598 to 0.003, but that for low Ri it cannot be the only transport mechanism (i.e. complementary
599 mechanisms being, for example, wind advection and turbulent diffusion). This explains, for
600 example, why the crosswind spreading can be described by a linear combination of

601 gravitational spreading and turbulent diffusion and not by gravitational spreading only (Fig.
602 11). The decrease with distance from vent of the relative contribution of the gravitational
603 spreading to the total cloud spreading cannot be appreciated at the range of observed
604 distances (150-300 km and 600-950 km for June 4 and 6), as it remains constant between 49-
605 71% and 40-50% associated with minimum and maximum volumetric flow rate of June 4 and
606 6, respectively (standard deviation <2%).

607 We suggest that, even for low Richardson number and low MFR, cloud downwind
608 velocity of the Cordón Caulle eruption was characterized by an important gravitational
609 component at least during the first few days (June 4-6) and the crosswind spreading (i.e. cloud
610 width) can be described by a linear combination of both gravitational spreading and turbulent
611 diffusion, with diffusion coefficients that are more consistent with observations (i.e. $\sim 9,000$
612 $\text{m}^2 \text{s}^{-1}$) (Figs. 11 and 12). This suggests that gravitational spreading, already shown to be crucial
613 to cloud development of strong plumes (e.g. Mt St Helens 1980, *Bonadonna and Phillips*
614 [2003]; Pinatubo 1991, *Costa et al.* [2013]; Plinian supereruption at Yellowstone volcano;
615 Mastin et al. [2014]), seems to describe also medial-to-distal spreading (100-1000 km) of
616 plumes characterized by relatively low MFR (10^6 - 10^7 kg s^{-1}).

617

618 **6. Conclusions**

619 Based on our detailed field campaigns and analytical studies we can conclude that:

- 620 1) The 2011 Cordón Caulle eruption started on June 4 and was characterized by a ~ 1 -day-long
621 climactic phase associated with a ~ 9 - 12 km high plume (above vent) and a peak MFR of
622 $\sim 10^7 \text{ kg s}^{-1}$ (June 4-5; Units I; average MFR of $\sim 7 \times 10^6 \text{ kg s}^{-1}$). For the following 10 days MFR
623 largely fluctuated but was always $> 10^6 \text{ kg s}^{-1}$ (June 5-14; Units II, III and IV; average MFR of
624 $3 \times 10^6 \text{ kg s}^{-1}$), while the second half of June was characterized by MFR $< 10^6 \text{ kg s}^{-1}$ (June 15-

625 30; average of $2 \times 10^5 \text{ kg s}^{-1}$). Average MFR between June 4 and 30 is $2 \times 10^6 \text{ kg s}^{-1}$. The activity
626 after June 30 was characterized by a several-month long period of low-intensity plumes.
627 Only the first plume on June 4 could be classified as subplinian, while the rest of the
628 eruption could be defined as small-moderate based on MFR, $Md\phi$ and LL plots.

629 2) The height of plumes is clearly controlled by their interaction with the atmosphere, and,
630 therefore, cannot be used as the sole indicator of eruptive conditions at the vent. The
631 scaling parameter Π helps discriminate between strong ($\Pi > 10$), transitional ($0.1 < \Pi < 10$)
632 and weak plumes ($\Pi < 0.1$). Nonetheless, the boundary values of 0.01 and 10 are to be
633 considered as comparative more than absolute, as the calculation of Π strongly depends
634 on the choice of entrainment coefficients.

635 3) Some of the plumes generated during the 2011 Cordón Caulle eruption, and, in particular,
636 those of the climactic phase (i.e., June 4-5), exhibit transitional features between strong-
637 and weak-plume dynamics with the timescale for wind entrainment term being about 6-8
638 times faster than the timescale for plume rise in a wind-still environment (i.e. $\Pi = 0.1-0.2$).
639 The periods of June 7-12, 14-19 and 23-30 were associated with weak plumes (i.e. $\Pi = 0.02-$
640 0.1).

641 4) As shown by satellite images, the sustained plume associated with the first few days of the
642 Cordón Caulle eruption was associated with a series of discrete pulses, which is typical of
643 long-lasting eruptions. Individual pulses could produce puffs with variable height above
644 the ground, which can increase the uncertainty in plume-height detection (e.g. June 4,
645 2011).

646 5) The VEI and Magnitude scale should be used with caution for long-lasting eruptions and
647 associated values depend on the number of phases considered. Individual layers (i.e., H
648 and K2) range between VEI 3-4, while the cumulative deposit associated with June 4-7,

649 2011 period of the Cordón Caulle eruption can be classified with a VEI 4-5 and a minimum
650 magnitude of 4.8 (including A-F, H and K2 layers; i.e., total mass/volume of $6.0 \pm 1.1 \times 10^{11}$
651 kg/ 1.1 ± 0.2 km³).

652 6) Crosswind cloud velocity of June 4 (between 160-270 km from vent), June 6 (NE cloud) and
653 June 6 (SE cloud) (between 580-950 km from vent) is between 6-10 m s⁻¹, 1-2 m s⁻¹ and 0-
654 1 m s⁻¹, respectively. Downwind cloud velocity of June 4 and 6 (NE cloud) is between 35-45
655 and 17-21 m s⁻¹, respectively.

656 7) Cloud spreading associated with transitional plumes, such as those of June 4 and 6, can be
657 described as a combination of gravitational intrusion, turbulent diffusion and wind
658 advection. In particular, crosswind spreading for both days can be best described by a
659 linear combination of gravitational spreading and turbulent diffusion with diffusion
660 coefficients in the range of expected values for diffusivity (i.e. 9,000 m² s⁻¹); relative
661 contribution is 49-71% and 40-50% for June 4 and 6, respectively, with no significant
662 variation with distance from vent. Downwind spreading can be described by a linear
663 combination of gravitational spreading and wind advection, with a relative contribution
664 between 8-19% and 5-9% of total spreading for the two days, respectively.

665 8) Our results indicate how the contribution of gravitational spreading can be significant even
666 for small-moderate eruptions characterized by transitional plumes strongly advected by
667 wind and associated with low Richardson number (e.g., 0.003-0.05) and relatively low MFR
668 (e.g., 10^6 - 10^7 kg s⁻¹); in the case of the first few days of the Cordón Caulle eruption such a
669 contribution is relevant even in medial-to-distal regions (100-1000 km from vent).

670 9) Detailed stratigraphic studies need to be combined with multiple modelling approaches in
671 order to best characterize complex volcanic activity, such as long-lasting eruptions
672 characterized by variable styles and interaction with the surrounding atmosphere.

673

674 **Acknowledgments**

675 C. Bonadonna was supported by Swiss National Science Foundation (SNSF; No
676 200020_125024). M. Pistolesi and R. Cioni were supported by Italian Ministero Universita' e
677 Ricerca funds (PRIN 2008 – AshErupt project). Authors are grateful to A. Bertagnini, R.
678 Gonzales, L. Francalanci and P. Sruoga for their assistance in the field and to S. Biass for the
679 analysis of ECMWF wind data. The associate Editor (M. Poland), L. Mastin and A. Folch are
680 thanked for the thorough and constructive reviews that significantly improved the original
681 manuscript. Data to support this article are available in the Supporting Information.

682 **References**

683
684 Alfano, F., C. Bonadonna, A. C. M. Volentik, C. B. Connor, S. F. L. Watt, D. M. Pyle, and L. J. Connor
685 (2011), Tephra stratigraphy and eruptive volume of the May, 2008, Chaiten eruption, Chile, *Bulletin*
686 *of Volcanology*, 73(5), 613-630, doi: 10.1007/s00445-010-0428-x.
687 Bonadonna, C., and J. C. Phillips (2003), Sedimentation from strong volcanic plumes, *Journal of*
688 *Geophysical Research*, 108(B7), 2340-2368.
689 Bonadonna, C., and A. Costa (2012), Estimating the volume of tephra deposits: A new simple strategy,
690 *Geology*, 40(5), 415-418, doi: 10.1130/g32769.1.
691 Bonadonna, C., and A. Costa (2013a), Plume height, volume, and classification of explosive volcanic
692 eruptions based on the Weibull function, *Bulletin of Volcanology*, 75(8), doi: 10.1007/s00445-013-
693 0742-1.
694 Bonadonna, C., and A. Costa (2013b), Modeling of tephra sedimentation from volcanic plumes, in
695 *Modeling Volcanic Processes: The Physics and Mathematics of Volcanism*, edited by S. Fagents, T.
696 Gregg and R. Lopes, Cambridge University Press.
697 Bonadonna, C., J. C. Phillips, and B. F. Houghton (2005a), Modeling tephra sedimentation from a
698 Ruapehu weak plume eruption, *Journal of Geophysical Research*, 110(B8, B08209).
699 Bonadonna, C., R. Cioni, M. Pistolesi, M. Elissondo, and V. Baumann (2015), Sedimentation of long-
700 lasting wind-affected volcanic plumes: the example of the 2011 rhyolitic Cordón Caulle eruption,
701 Chile, *Bulletin of Volcanology*, doi: 10.1007/s00445-015-0900-8.
702 Bonadonna, C., R. Cioni, A. Costa, T. H. Druitt, J. C. Phillips, and L. Pioli (2014), MeMoVolc workshop
703 on the "Dynamics of volcanic explosive eruptions", Consensual Document,
704 <https://vhub.org/resources/3561>.
705 Bonadonna, C., C. B. Connor, B. F. Houghton, L. Connor, M. Byrne, A. Laing, and T. Hincks (2005b),
706 Probabilistic modeling of tephra dispersion: hazard assessment of a multi-phase eruption at
707 Tarawera, New Zealand, *Journal of Geophysical Research*, 110(B3, B03203).
708 Bonadonna, C., R. Cioni, M. Pistolesi, C. B. Connor, S. Scollo, L. Pioli, and M. Rosi (2013), Determination
709 of the largest clast sizes of tephra deposits for the characterization of explosive eruptions: a study
710 of the IAVCEI commission on tephra hazard modelling, *Bulletin of Volcanology*, 75(1), doi:
711 10.1007/s00445-012-0680-3.
712 Briggs, G. A. (1972), Chimney plumes in neutral and stable surroundings, *Atmospheric Environment*,
713 6(7), 507-516, doi: 10.1016/0004-6981(72)90120-5.
714 Bursik, M. (1998), Tephra dispersal, in *The physics of explosive volcanic eruptions*, edited by J. S. Gilbert
715 and R. S. J. Sparks, pp. 115-144, The Geological Society, London.
716 Bursik, M. (2001), Effect of wind on the rise height of volcanic plumes, *Geophysical Research Letter*,
717 28(18), 3621-3624.
718 Carazzo, G., E. Kaminski, and S. Tait (2008), On the rise of turbulent plumes: Quantitative effects of
719 variable entrainment for submarine hydrothermal vents, terrestrial and extra terrestrial explosive
720 volcanism, *Journal of Geophysical Research-Solid Earth*, 113(B9), doi: 10.1029/2007jb005458.
721 Carazzo, G., F. Girault, T. Aubry, H. Bouquerel, and K. E. (2014), Laboratory experiments of forced
722 plumes in a density-stratified crossflow and implications for volcanic plumes, doi:
723 10.1002/2014GL061887
724 Castro, J. M., and D. B. Dingwell (2009), Rapid ascent of rhyolitic magma at Chaiten volcano, Chile,
725 *Nature*, 461(7265), 780-U729, doi: 10.1038/nature08458.
726 Castro, J. M., C. I. Schipper, S. P. Mueller, A. S. Militzer, A. Amigo, C. Silva Parejas, and D. Jacob (2013),
727 Storage and eruption of near-liquidus rhyolite magma at Cordón Caulle, Chile, *Bulletin of*
728 *Volcanology*, 75(4), doi: 10.1007/s00445-013-0702-9.
729 Collini, E., S. M. Osorio, A. Folch, J. G. Viramonte, G. Villarosa, and G. Salmuni (2013), Volcanic ash
730 forecast during the June 2011 Cordón Caulle eruption, *Natural Hazards*, 66(2), 389-412, doi:
731 10.1007/s11069-012-0492-y.

732 Connor, L. G., and C. B. Connor (2006), Inversion is the key to dispersion: understanding eruption
733 dynamics by inverting tephra fallout, in *Statistics in Volcanology*, edited by H. Mader, S. Cole, C. B.
734 Connor and L. G. Connor, pp. 231-242, Geological Society London.

735 Contini, D., A. Donato, D. Cesari, and A. G. Robins (2011), Comparison of plume rise models against
736 water tank experimental data for neutral and stable crossflows, *Journal of Wind Engineering and*
737 *Industrial Aerodynamics*, 99(5), 539-553, doi: 10.1016/j.jweia.2011.02.003.

738 Costa, A., A. Folch, and G. Macedonio (2013), Density-driven transport in the umbrella region of
739 volcanic clouds: Implications for tephra dispersion models, *Geophysical Research Letters*, 40(18),
740 4823-4827, doi: 10.1002/grl.50942.

741 Dee, D. P., et al. (2011), The ERA-Interim reanalysis: configuration and performance of the data
742 assimilation system, *Quarterly Journal of the Royal Meteorological Society*, 137(656), 553-597, doi:
743 10.1002/qj.828.

744 Degruyter, W., and C. Bonadonna (2012), Improving on mass flow rate estimates of volcanic eruptions,
745 *Geophysical Research Letters*, 39, doi: 10.1029/2012gl052566.

746 Degruyter, W., and C. Bonadonna (2013), Impact of wind on the condition for column collapse of
747 volcanic plumes, *Earth and Planetary Science Letters*, 377, 218-226, doi:
748 10.1016/j.epsl.2013.06.041.

749 Devenish, B. J. (2013), Using simple plume models to refine the source mass flux of volcanic eruptions
750 according to atmospheric conditions, *Journal of Volcanology and Geothermal Research*, 256, 118-
751 127, doi: 10.1016/j.jvolgeores.2013.02.015.

752 Devenish, B. J., G. G. Rooney, H. N. Webster, and D. J. Thomson (2010), The Entrainment Rate for
753 Buoyant Plumes in a Crossflow, *Boundary-Layer Meteorology*, 134(3), 411-439, doi:
754 10.1007/s10546-009-9464-5.

755 Dufek, J., M. Manga, and M. Staedter (2007), Littoral blasts: Pumice-water heat transfer and the
756 conditions for steam explosions when pyroclastic flows enter the ocean, *Journal of Geophysical*
757 *Research-Solid Earth*, 112(B11), doi: 10.1029/2006jb004910.

758 Fierstein, J., and W. Hildreth (1992), The plinian eruptions of 1912 at Novarupta, Katmai National Park,
759 Alaska, *Bulletin of Volcanology*, 54, 646-684.

760 Folch, A., O. Jorba, and J. Viramonte (2008), Volcanic ash forecast - application to the May 2008
761 Chaiten eruption, *Natural Hazards and Earth System Sciences*, 8(4), 927-940.

762 Fontijn, K., G. G. J. Ernst, C. Bonadonna, M. A. Elburg, E. Mbede, and P. Jacobs (2011), The 4-ka Rungwe
763 Pumice (South-Western Tanzania): a wind-still Plinian eruption, *Bulletin of Volcanology*, 73(9),
764 1353-1368, doi: 10.1007/s00445-011-0486-8.

765 Heffter, J. L. (1965), The variation of horizontal diffusion parameters with time for travel periods of
766 one hour or longer, *J. Appl. Meteorol.*, 4(1), 153-156.

767 Hewett, T. A., J. A. Fay, and D. P. Hoult (1971), Laboratory experiments of smokestack plumes in a
768 stable atmosphere, *Atmospheric Environment*, 5(9), 767-&, doi: 10.1016/0004-6981(71)90028-x.

769 Holasek, R. E., and S. Self (1995), Goes Weather-Satellite Observations and Measurements of the May
770 18, 1980, Mount-St-Helens Eruption, *Journal of Geophysical Research-Solid Earth*, 100(B5), 8469-
771 8487.

772 Huq, P., and E. J. Stewart (1996), A laboratory study of buoyant plumes in laminar and turbulent
773 crossflows, *Atmospheric Environment*, 30(7), 1125-1135, doi: 10.1016/1352-2310(95)00335-5.

774 Jay, J., F. Costa, M. Pritchard, L. E. Lara, B. Singer, and J. Herrin (2014), Locating magma reservoirs using
775 InSAR and petrology before and during the 2011–2012 Cordón Caulle silicic eruption, *Earth and*
776 *Planetary Science Letters*, 395, 254-266.

777 Mastin, L. G. (2014), Testing the accuracy of a 1-D volcanic plume model in estimating mass eruption
778 rate, *Journal of Geophysical Research-Atmospheres*, 119(5), 2474-2495, doi:
779 10.1002/2013jd020604.

780 Mastin, L. G., A. R. Van Eaton, and J. B. Lowenstern (2014), Modeling ash fall distribution from a
781 Yellowstone supereruption, *Geochemistry Geophysics Geosystems*, 15(8), 3459-3475, doi:
782 10.1002/2014gc005469.

783 Mastin, L. G., et al. (2009), A multidisciplinary effort to assign realistic source parameters to models of
784 volcanic ash-cloud transport and dispersion during eruptions, *Journal of Volcanology and*
785 *Geothermal Research*, 186(1-2), 10-21, doi: 10.1016/j.jvolgeores.2009.01.008.

786 Morton, B., G. L. Taylor, and J. S. Turner (1956), Turbulent gravitational convection from maintained
787 and instantaneous source, *Proceedings of the Royal Society*, 234, 1-23.

788 Newhall, C. G., and S. Self (1982), The Volcanic Explosivity Index (Vei) - an Estimate of Explosive
789 Magnitude for Historical Volcanism, *Journal of Geophysical Research-Oceans and Atmospheres*,
790 87(NC2), 1231-1238.

791 Oddsson, B., M. T. Gudmundsson, G. Larsen, and S. Karlsdottir (2012), Monitoring of the plume from
792 the basaltic phreatomagmatic 2004 Grimsvotn eruption-application of weather radar and
793 comparison with plume models, *Bulletin of Volcanology*, 74(6), 1395-1407, doi: 10.1007/s00445-
794 012-0598-9.

795 Pasquill, F. (1974), *Atmospheric Diffusion*, second ed., John Wiley & Sons, Chichester.

796 Pistolesi, M., R. Cioni, C. Bonadonna, M. Elissondo, V. Baumann, A. Bertagnini, L. Chiari, R. Gonzales,
797 M. Rosi, and L. Francalanci (2015), Complex dynamics of small-moderate volcanic events: the
798 example of the 2011 rhyolitic Cordón Caulle eruption, Chile, *Bulletin of Volcanology*, doi:
799 10.1007/s00445-014-0898-3.

800 Prejean, S. G., and E. E. Brodsky (2011), Volcanic plume height measured by seismic waves based on a
801 mechanical model, *Journal of Geophysical Research-Solid Earth*, 116, doi: 10.1029/2010jb007620.

802 Pyle, D. M. (1989), The thickness, volume and grainsize of tephra fall deposits, *Bulletin of Volcanology*,
803 51(1), 1-15.

804 Pyle, D. M. (2000), Sizes of volcanic eruptions, in *Encyclopedia of volcanoes*, edited by H. Sigurdsson,
805 B. Houghton, S. McNutt, H. Rymer and J. Stix, Academic Press.

806 Ripepe, M., C. Bonadonna, A. Folch, D. Delle Donne, G. Lacanna, E. Marchetti, and A. Hoeskuldsson
807 (2013), Ash-plume dynamics and eruption source parameters by infrasound and thermal imagery:
808 The 2010 Eyjafjallajokull eruption, *Earth and Planetary Science Letters*, 366, 112-121, doi:
809 10.1016/j.epsl.2013.02.005.

810 Scollo, S., S. Tarantola, C. Bonadonna, M. Coltelli, and A. Saltelli (2008), Sensitivity analysis and
811 uncertainty estimation for tephra dispersal models, *Journal of Geophysical Research-Solid Earth*,
812 113(B6), doi: 10.1029/2006jb004864.

813 SERNAGEOMIN/OVDAS (2011), Puyehue - Cordón Caulle: Reporte especial de actividad volcánica
814 No31Rep., <http://www.sernageomin.cl/volcan.php?pagina=7&ild=38>.

815 Siebert, L., T. Simkin, and P. Kimberly (2010), *Volcanoes of the world*, University of California Press,
816 Berkeley.

817 Sparks, R. S. J., M. I. Bursik, S. N. Carey, J. S. Gilbert, L. S. Glaze, H. Sigurdsson, and A. W. Woods (1997),
818 *Volcanic Plumes*, 574 pp., John Wiley & Sons, Chichester.

819 Suzuki, Y. J., and T. Koyaguchi (2010), Numerical determination of the efficiency of entrainment in
820 volcanic eruption columns, *Geophysical Research Letters*, 37, doi: 10.1029/2009gl042159.

821 Suzuki, Y. J., and T. Koyaguchi (2013), 3D numerical simulation of volcanic eruption clouds during the
822 2011 Shinmoe-dake eruptions, *Earth Planets and Space*, 65(6), 581-589, doi:
823 10.5047/eps.2013.03.009.

824 Tuffen, H., M. R. James, J. M. Castro, and C. I. Schipper (2013), Exceptional mobility of an advancing
825 rhyolitic obsidian flow at Cordon Caulle volcano in Chile, *Nature Communications*, 4, doi:
826 10.1038/ncomms3709.

827 Tupper, A., and R. Wunderman (2009), Reducing discrepancies in ground and satellite-observed
828 eruption heights, *Journal of Volcanology and Geothermal Research*, 186(1-2), 22-31, doi:
829 10.1016/j.jvolgeores.2009.02.015.

830 Valentine, G. A., and K. H. Wohletz (1989), Numerical-models of plinian eruption columns and
831 pyroclastic flows, *Journal of Geophysical Research-Solid Earth and Planets*, 94(B2), 1867-1887, doi:
832 10.1029/JB094iB02p01867.

833 Volentik, A. C. M., C. Bonadonna, C. B. Connor, L. J. Connor, and M. Rosi (2010), Modeling tephra
834 dispersal in absence of wind: Insights from the climactic phase of the 2450 BP Plinian eruption of
835 Pululagua volcano (Ecuador), *Journal of Volcanology and Geothermal Research*, 193(1-2), 117-136,
836 doi: 10.1016/j.jvolgeores.2010.03.011.

837 Walker, G. P. L., and R. Croasdale (1971), Two plinian-type eruptions in the Azores, *Journal of the*
838 *Geological Society of London*, 127, 17-55.

839 Whittington, A. G., A. M. Hofmeister, and P. I. Nabelek (2009), Temperature-dependent thermal
840 diffusivity of the Earth's crust and implications for magmatism, *Nature*, 458(7236), 319-321, doi:
841 10.1038/nature07818.

842 Wicks, C., J. Carlos de la Llera, L. E. Lara, and J. Lowenstern (2011), The role of dyking and fault control
843 in the rapid onset of eruption at Chaiten volcano, Chile, *Nature*, 478(7369), 374-+, doi:
844 10.1038/nature10541.

845 Woodhouse, M. J., A. J. Hogg, J. C. Phillips, and R. S. J. Sparks (2013), Interaction between volcanic
846 plumes and wind during the 2010 Eyjafjallajokull eruption, Iceland, *Journal of Geophysical*
847 *Research-Solid Earth*, 118(1), 92-109, doi: 10.1029/2012jb009592.

848 Woods, A. W. (1988), The fluid-dynamics and thermodynamics of eruption columns, *Bulletin of*
849 *Volcanology*, 50(3), 169-193.

850

851

852

853 **Figure captions**

854 **Fig. 1** Volcanic plumes associated with the 2011 eruption of Cordón Caulle: **a)** June 4, plume height
855 of ~9-12 km above the vent (also showing pyroclastic density currents), **b)** and **c)** June 13, plume
856 height of ~7-9 km above the vent (a- [http://www.emol.com/noticias/
857 internacional/2011/06/15/487543/miles-de-pasajeros-atrapados-en-nueva-zelanda-y-australia-por-
858 ceniza-del-volcan-puyehue.html](http://www.emol.com/noticias/internacional/2011/06/15/487543/miles-de-pasajeros-atrapados-en-nueva-zelanda-y-australia-por-ceniza-del-volcan-puyehue.html); b- <http://imagenesfotos.com/fotos-del-volcan-puyehue/> and c-
859 <http://www.flickr.com/photos/pentadragon/>).

860 **Fig. 2** Isopleth map (in cm) of the largest lithics (LL) for Unit I (layers A-F) based on: **a)** the geometric
861 mean of the 5 largest clasts; **b)** the 50th percentile of a 20-clast population.

862 **Fig. 3** Md ϕ map for Unit I (cumulative layer A-F) (units in ϕ).

863 **Fig. 4** Plot of Log(erupted mass) vs. plume height (km) (above sea level) showing the minimum
864 values of the goodness-of-fit measure (Root Mean Square Error, RMSE; kg/m²) for the tephra deposit
865 associated with: **a)** layer A-B, **b)** layer A-F and **c)** layer A-F (coarse fraction: -5 to 3 ϕ). Erupted mass
866 was varied between 10⁸ and 10¹³ kg with 0.2-log(mass) increments and the plume height was varied
867 between 6 and 22 km with 2-km-height increments. Resulting values were interpolated to produce
868 2D RMSE. A scale of RMSE is also shown, with dark blue indicating the minimum values (i.e. best fit).
869 Vertical dashed lines indicate the interval of erupted mass as obtained from empirical integrations
870 (Table 1), while horizontal dashed lines indicate the range of observed plume heights (Supporting
871 Information). Erupted mass of the coarse fraction of layer A-F is calculated as 85% of total mass from
872 grain-size analysis of *Bonadonna et al.* [2015].

873 **Fig. 5** Examples of plumes taken from the Futangue stationary camera on June 13, 14 and 20, 2011
874 **a)** to **c)** and **d)** Moderate Resolution Imaging Spectroradiometer (MODIS) image of the Aqua satellite
875 captured shortly after the beginning of the eruption on June 4
876 (<http://www.earthobservatory.nasa.gov/NaturalHazards/event.php?id=50859>).

877 **e)** Variation with time (June 4-30, 2011) of plume height above sea level (from GVP) and wind speed
878 (ECMWF). Vertical and horizontal error bars indicate the uncertainty associated with the detection
879 of plume height and with the timing of plume height detection as reported by *Collini et al.* [2013]
880 and GVP, respectively. Horizontal dashed line in plot (e) is vent height.

881 **Fig. 6** Variation with time (June 4-30, 2011) of MFR as determined based on the equation of
882 *Degruyter and Bonadonna* [2012] (eq. 1 in main text). Blue rectangles indicate the variation range of
883 MFR associated with uncertainty on plume height and atmospheric conditions as shown in Fig. 5
884 (radial entrainment, wind entrainment and eruption temperature were fixed to 0.1, 0.5 and 894 °C,
885 respectively). White rectangles indicate the variation range of MFR including all sources of
886 uncertainty (i.e. using extreme values for height, atmospheric profiles, entrainment rates and source
887 temperature; see text for details). Black circles indicate the log average of the minimum and
888 maximum value of the blue rectangles. Horizontal blue line indicates MFR of 10⁶ kg s⁻¹.

889 **Fig. 7 a)** Simplified sketch illustrating strong, transitional and weak plumes based on the scaling
890 parameter Π and **b)** variation of Π with time as determined with the equation of *Degruyter and*
891 *Bonadonna* [2012] (eq. 2 in main text). See caption of Fig. 6 for descriptions of symbols. Horizontal

892 dashed blue lines indicate fields of strong ($\Pi > 10$), transitional ($0.1 < \Pi < 10$) and weak plumes ($\Pi < 0.1$),
893 respectively. Vertical blue line indicates the transition between the periods characterized by MFR $>$
894 and $<$ of 10^6 kg s^{-1} .

895 **Fig. 8.** Classification of the Cordón Caulle eruption based on the plume height versus MFR plot of
896 *Bonadonna and Costa* [2013] showing a combination of subplinian (blue star; June 4, 2011) and
897 small-moderate plumes (yellow stars; June 5-30, 2011) of the Cordón Caulle eruption. Plume height
898 is indicated as average of observations above the vent (km) and MFR is calculated based on the
899 model of *Degruyter and Bonadonna* [2012] (black circles in Fig. 6). All MFR estimates are within a
900 factor 10 (red solid lines) from the *Mastin et al.* [2009] estimates (red squares). The horizontal and
901 vertical error bars on the red squares indicate a typical 20% error on the calculation of plume height
902 and a typical MFR spreading of a factor 4 as indicated by *Mastin et al.* [2009], respectively.

903 **Fig. 9.** Classification of the Unit I (A-F cumulative layer; black squares) based on the Weibull fit for: **a)**
904 thinning versus largest clast trend (λ_{th} and λ_{LL}) and **b)** thinning versus $Md\phi$ trend (λ_{th} and $\lambda_{Md\phi}$)
905 (adjusted from *Bonadonna and Costa* [2013]). Red, black, green and blue solid lines represent
906 theoretical lines for Ht of 41, 24, 14 and 10 km based on the empirical equations of λ_{LL} and $\lambda_{Md\phi}$
907 versus plume height for plot a) and b) respectively. Dashed lines indicate a 20% error in the
908 calculation of plume height. Error bars of 30, 50 and 40% are also shown for the estimation of λ_{th} ,
909 $\lambda_{LL}/\lambda_{th}$, and $\lambda_{Md\phi}/\lambda_{th}$ respectively (as taken from *Bonadonna and Costa* [2013]). Examples of Plinian to
910 Ultraplinian (i.e. Taupo, Hatepe, Tarawera, Cotopaxi Layer 3, Cotopaxi Layer 5, Pululagua) and
911 subplinian to small-moderate eruptions (i.e. Vesuvius 512, Averno A1 to A6, Boqueron C) are also
912 shown (orange circles; see *Bonadonna and Costa* [2013] for more details).

913 **Fig. 10** Downwind and crosswind extension of the volcanic clouds developed on **a)** June 4, 2011 and
914 **b)** June 6, 2011 as observed from the GOES satellite images for the time interval 18:45-20:15 UTC
915 and 12:45-19:45 UTC respectively (total measurement uncertainty includes pixel size of these GOES
916 images, i.e. $\sim 2 \text{ km}$, and definition of cloud boundaries, i.e. $\sim 5 \text{ km}$). On June 6 two distinct clouds
917 developed: one moving towards NE and one moving towards SE.

918 **Fig. 11** Variation of downwind distance from vent versus width for: i) volcanic clouds developed on
919 both June 4 and 6 (NE cloud) as observed from satellite images (violet and red squares, respectively;
920 from Fig. 10) and ii) 1 kg m^{-2} isoline of Unit I (blue diamonds; Supporting Information) described as:

921 **a)** gravitational spreading plus turbulent diffusion (for a best-fit diffusion coefficient of $9,000 \text{ m}^2 \text{ s}^{-1}$).
922 Dashed and solid lines are associated with minimum and maximum values of volumetric flow rate
923 (Q) at the neutral buoyancy level, respectively, related to variable plume height and atmospheric
924 conditions, i.e. $0.5\text{-}4.3 \times 10^9 \text{ m}^3 \text{ s}^{-1}$ (for the June 4 event) and $3.5\text{-}8.6 \times 10^8 \text{ m}^3 \text{ s}^{-1}$ (for the June 6 event)
925 (as calculated with the model of *Degruyter and Bonadonna* [2012]);

926 **b)** turbulent diffusion (eq. 5) for best-fit diffusion coefficients K ($\text{m}^2 \text{ s}^{-1}$) and wind velocity u (m s^{-1})
927 averaged between neutral buoyancy level and total plume height and between the volcano location
928 and the maximum extension of the observed cloud for June 4 and June 6 (indicated next to best-fit
929 lines); for simplicity, an average wind velocity of 29 m s^{-1} for minimum and maximum plume height
930 of June 4th was considered;

931 c) gravitational spreading (eq. 4 considering $\lambda=0.8$ and $N=0.01 \text{ s}^{-1}$; see *Bonadonna and Phillips* [2003]
932 for more details). Vertical bars indicate a 20% uncertainty on the calculated width in relation to the
933 cloud geometry (see *Bonadonna and Phillips* [2003] for more details).

934 **Fig. 12** Variation of spreading velocity in the downwind (blue diamonds) and crosswind (red squares)
935 directions at various distances from vent for: **a)** June 4, 2011 (observations between 18:45 and 20:15
936 UTC) and **b)** June 6, 2011 (observations between 12:45 and 19:45 UTC). Solid and dashed lines
937 indicate the wind velocity u (m s^{-1}) at each distance from vent for minimum and maximum plume
938 height (see Fig. 5 and Supporting Information for plume height data; only one height observation is
939 available for June 6). Wind data are averaged between the neutral buoyancy level and total plume
940 height for each cloud position. Circles and triangles indicate respectively the spreading velocity due
941 to buoyancy (u_b , as calculated for minimum and maximum values of Q from eq. 6 considering $\lambda=0.8$
942 and $N=0.01 \text{ s}^{-1}$) and the downwind velocity calculated as a combination between u_b and u . Q values
943 used in eq. 6 are described in caption of Fig. 11. Vertical bars indicate the uncertainty associated
944 with the observed velocity derived from an average cumulative error of $\pm 7\text{km}$ on the downwind and
945 crosswind lengths (see Fig. 10 for more details). A 25% uncertainty on the calculated minimum and
946 maximum cloud-spreading velocity due to buoyancy (u_b) is also shown (as estimated by *Bonadonna*
947 *and Phillips* [2003] in relation to the cloud geometry).

948

949

950

Figures



Fig. 1 Volcanic plumes associated with the 2011 eruption of Cordón Caulle: **a)** June 4, plume height of ~9-12 km above the vent (also showing pyroclastic density currents), **b)** and **c)** June 13, plume height of ~7-9 km above the vent (a- <http://www.emol.com/noticias/internacional/2011/06/15/487543/miles-de-pasajeros-atrapados-en-nueva-zelanda-y-australia-por-ceniza-del-volcan-puyehue.html>; b- <http://imagenesfotos.com/fotos-del-volcan-puyehue/> and c- <http://www.flickr.com/photos/pentadragon/>).

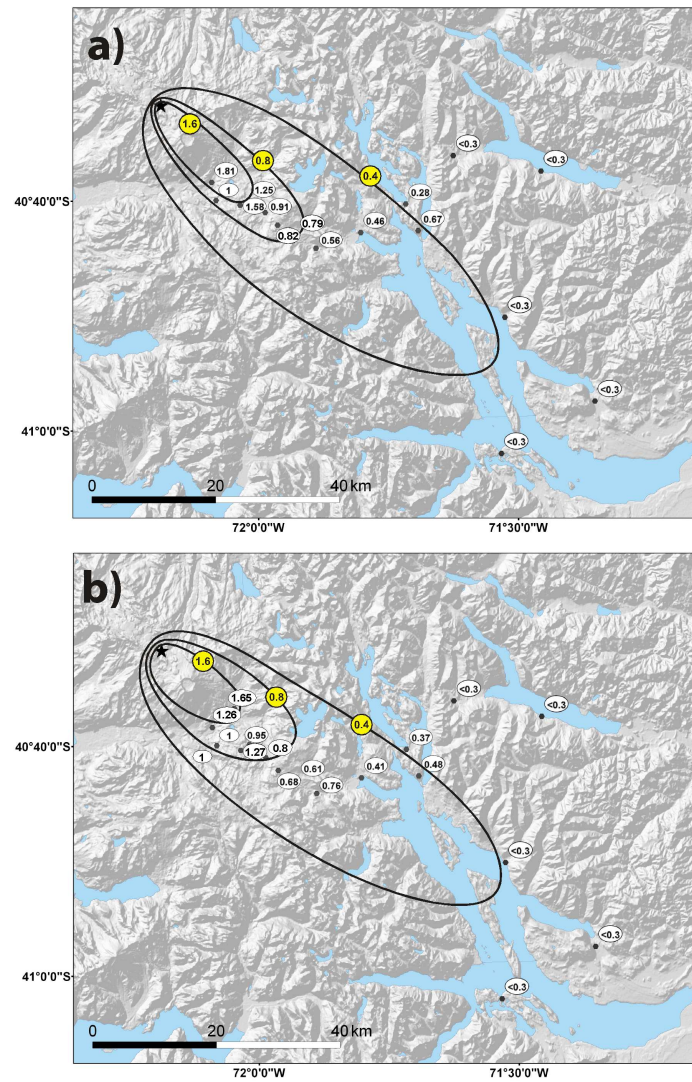


Fig. 2 Isopleth map (in cm) of the largest lithics (LL) for Unit I (layers A-F) based on: **a)** the geometric mean of the 5 largest clasts; **b)** the 50th percentile of a 20-clast population.

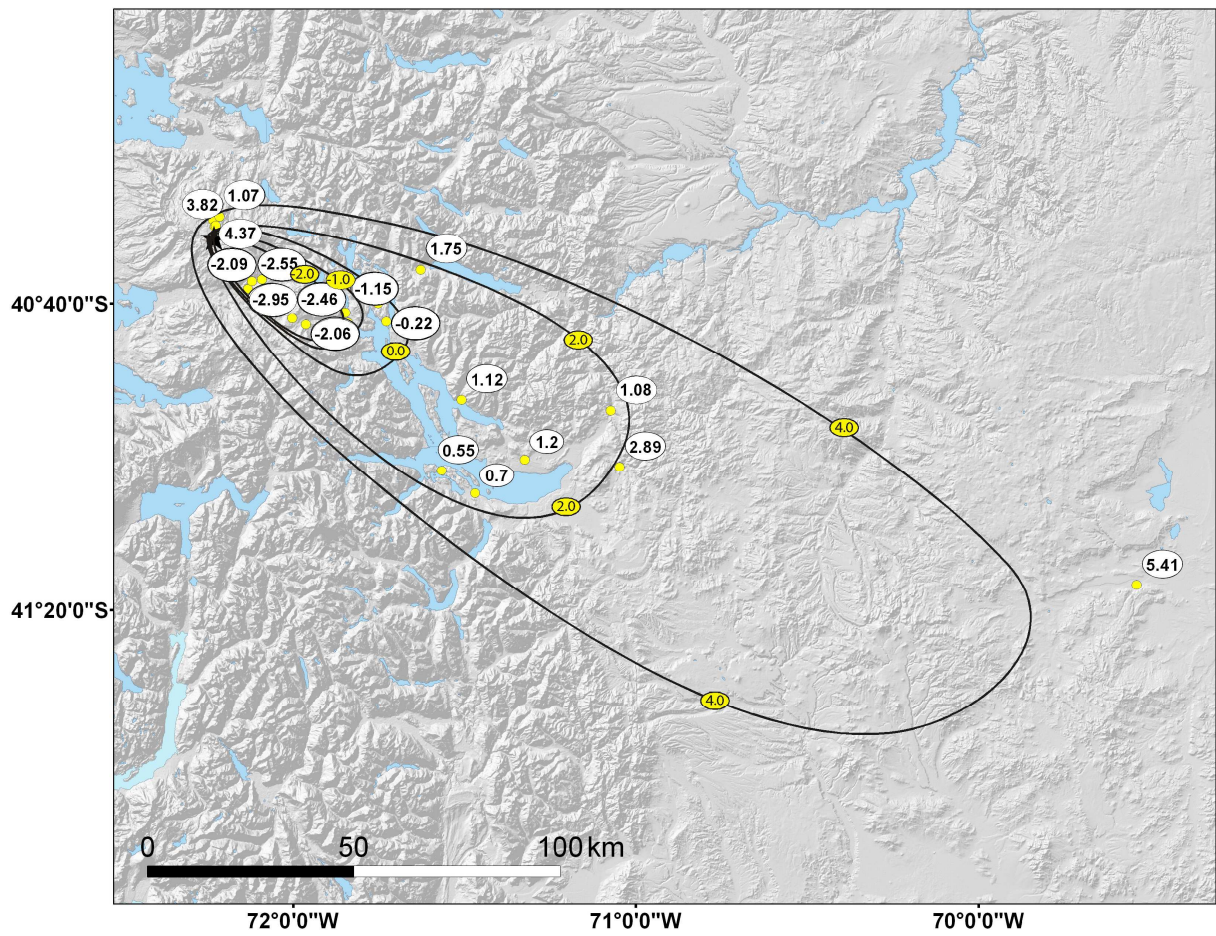


Fig. 3 $M\delta\phi$ map for Unit I (cumulative layer A-F) (units in ϕ).

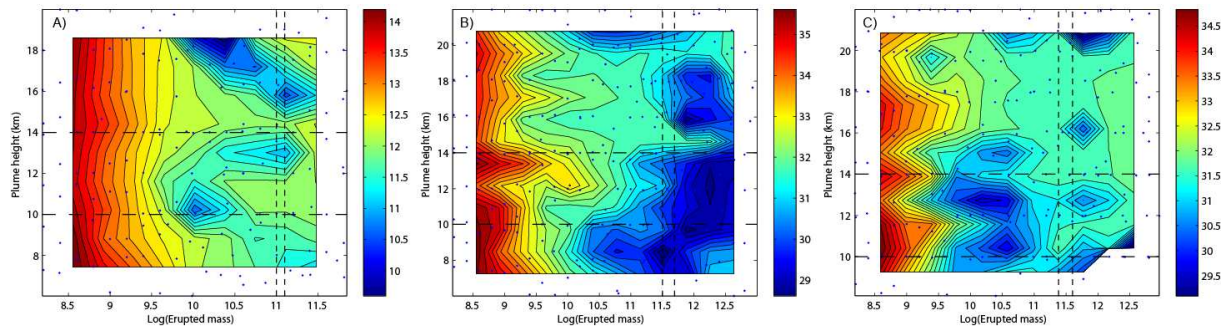


Fig. 4 Plot of Log(erupted mass) vs. plume height (km) (above sea level) showing the minimum values of the goodness-of-fit measure (Root Mean Square Error, RMSE; kg/m^2) for the tephra deposit associated with: **a)** layer A-B, **b)** layer A-F and **c)** layer A-F (coarse fraction: -5 to 3ϕ). Erupted mass was varied between 10^8 and 10^{13} kg with $0.2\text{-log}(\text{mass})$ increments and the plume height was varied between 6 and 22 km with 2-km-height increments. Resulting values were interpolated to produce 2D RMSE. A scale of RMSE is also shown, with dark blue indicating the minimum values (i.e. best fit). Vertical dashed lines indicate the interval of erupted mass as obtained from empirical integrations (Table 1), while horizontal dashed lines indicate the range of observed plume heights (Supporting Information). Erupted mass of the coarse fraction of layer A-F is calculated as 85% of total mass from grain-size analysis of *Bonadonna et al.* [2015].

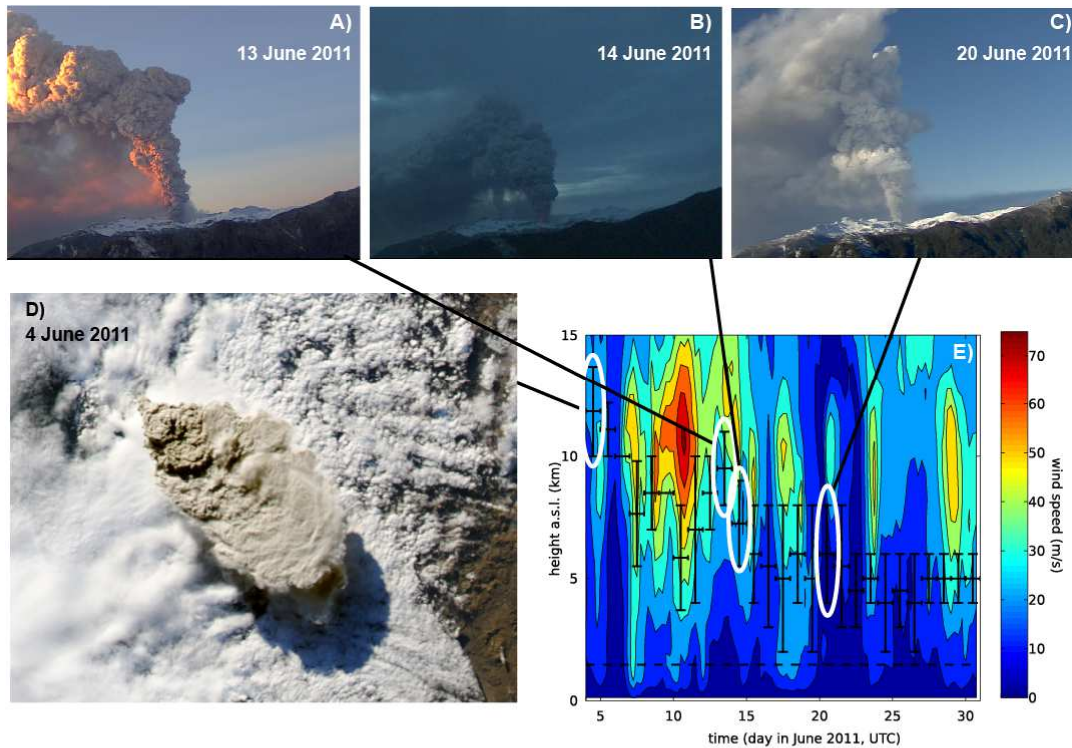


Fig. 5 Examples of plumes taken from the Futangue stationary camera on June 13, 14 and 20, 2011 (a to c) and d) Moderate Resolution Imaging Spectroradiometer (MODIS) image of the Aqua satellite captured shortly after the beginning of the eruption on June 4 (<http://www.earthobservatory.nasa.gov/NaturalHazards/event.php?id=50859>).

e) Variation with time (June 4-30, 2011) of plume height above sea level (from GVP) and wind speed (ECMWF). Vertical and horizontal error bars indicate the uncertainty associated with the detection of plume height and with the timing of plume height detection as reported by *Collini et al.* [2013] and GVP, respectively. Horizontal dashed line in plot (e) is vent height.

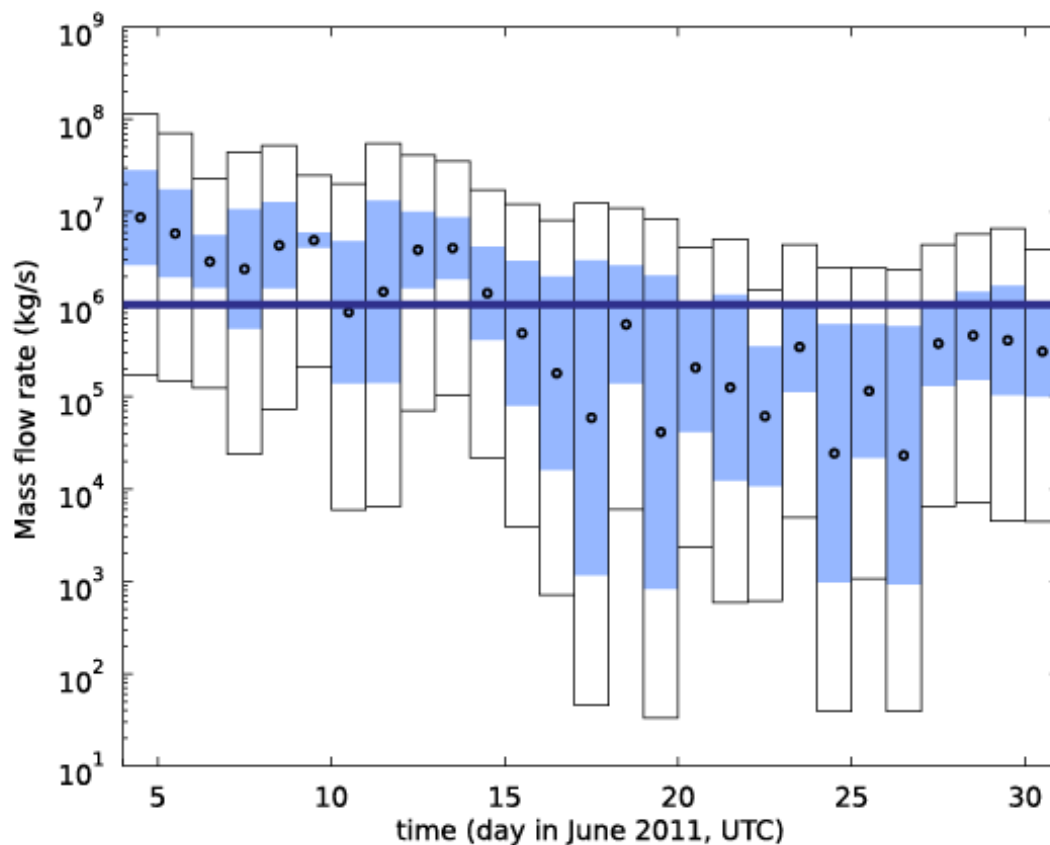


Fig. 6 Variation with time (June 4-30, 2011) of MFR as determined based on the equation of Degruyter and Bonadonna [2012] (eq. 1 in main text). Blue rectangles indicate the variation range of MFR associated with uncertainty on plume height and atmospheric conditions as shown in Fig. 5 (radial entrainment, wind entrainment and eruption temperature were fixed to 0.1, 0.5 and 894 °C, respectively). White rectangles indicate the variation range of MFR including all sources of uncertainty (i.e. using extreme values for height, atmospheric profiles, entrainment rates and source temperature; see text for details). Black circles indicate the log average of the minimum and maximum value of the blue rectangles. Horizontal blue line indicates MFR of 10^6 kg s⁻¹.

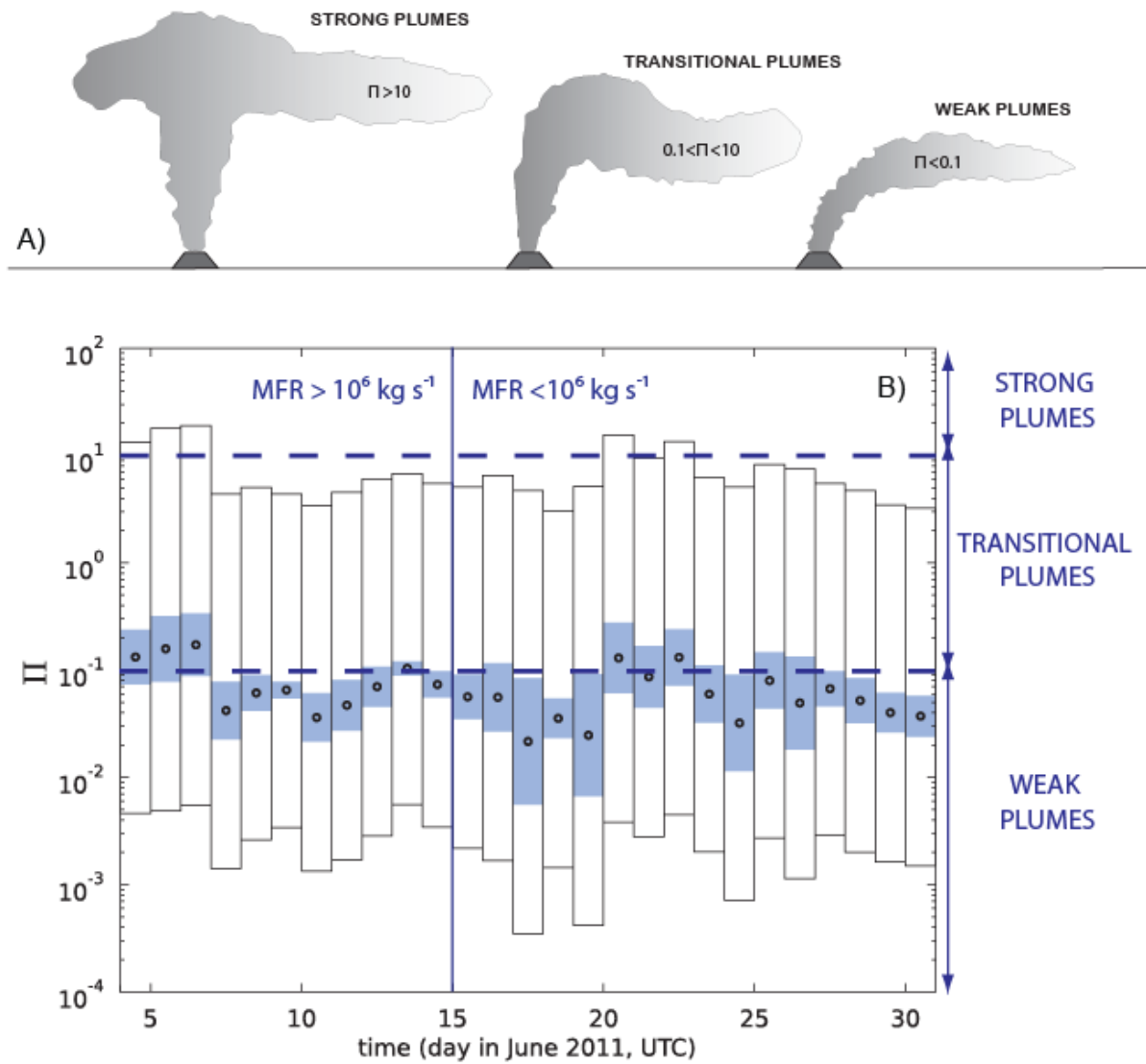


Fig. 7 **a)** Simplified sketch illustrating strong, transitional and weak plumes based on the scaling parameter Π and **b)** variation of Π with time as determined with the equation of *Degruyter and Bonadonna* [2012] (eq. 2 in main text). See caption of Fig. 6 for descriptions of symbols. Horizontal dashed blue lines indicate fields of strong ($\Pi > 10$), transitional ($0.1 < \Pi < 10$) and weak plumes ($\Pi < 0.1$), respectively. Vertical blue line indicates the transition between the periods characterized by $MFR >$ and $<$ of 10^6 kg s^{-1} .

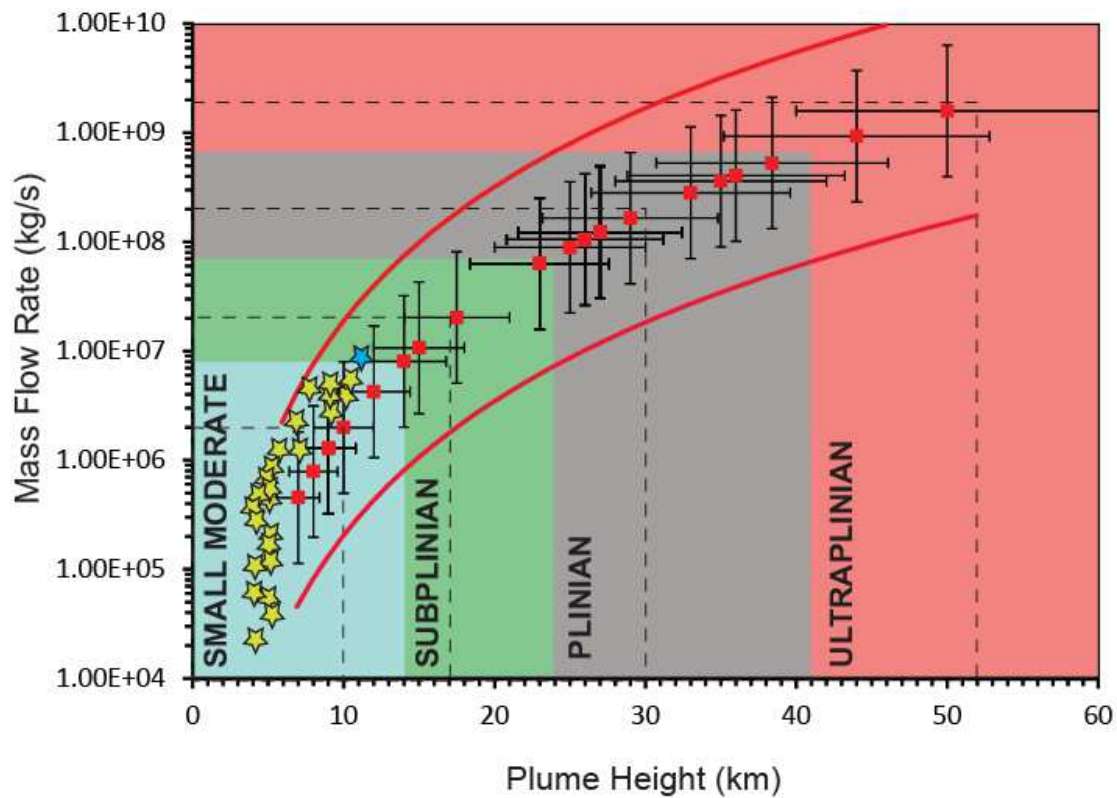


Fig. 8. Classification of the Cordón Caulle eruption based on the plume height versus MFR plot of *Bonadonna and Costa* [2013] showing a combination of subplinian (blue star; June 4, 2011) and small-moderate plumes (yellow stars; June 5-30, 2011) of the Cordón Caulle eruption. Plume height is indicated as average of observations above the vent (km) and MFR is calculated based on the model of *Degruyter and Bonadonna* [2012] (black circles in Fig. 6). All MFR estimates are within a factor 10 (red solid lines) from the *Mastin et al.* [2009] estimates (red squares). The horizontal and vertical error bars on the red squares indicate a typical 20% error on the calculation of plume height and a typical MFR spreading of a factor 4 as indicated by *Mastin et al.* [2009], respectively.

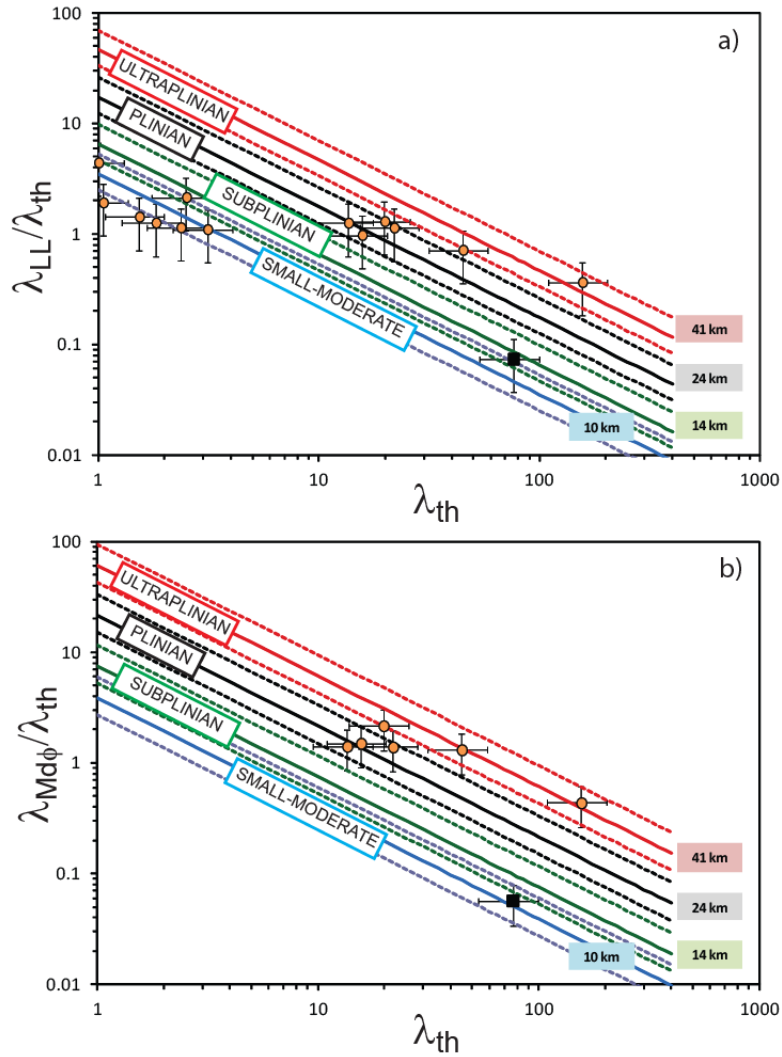


Fig. 9. Classification of the Unit I (A-F cumulative layer; black squares) based on the Weibull fit for: **a)** thinning versus largest clast trend (λ_{th} and λ_{LL}) and **b)** thinning versus Md ϕ trend (λ_{th} and $\lambda_{Md\phi}$) (adjusted from *Bonadonna and Costa* [2013]). Red, black, green and blue solid lines represent theoretical lines for Ht of 41, 24, 14 and 10 km based on the empirical equations of λ_{LL} and $\lambda_{Md\phi}$ versus plume height for plot a) and b) respectively. Dashed lines indicate a 20% error in the calculation of plume height. Error bars of 30, 50 and 40% are also shown for the estimation of λ_{th} , $\lambda_{LL}/\lambda_{th}$ and $\lambda_{Md\phi}/\lambda_{th}$ respectively (as taken from *Bonadonna and Costa* [2013]). Examples of Plinian to Ultraplinian (i.e. Taupo, Hatepe, Tarawera, Cotopaxi Layer 3, Cotopaxi Layer 5, Pululagua) and subplinian to small-moderate eruptions (i.e. Vesuvius 512, Averno A1 to A6, Boqueron C) are also shown (orange circles; see *Bonadonna and Costa* [2013] for more details).

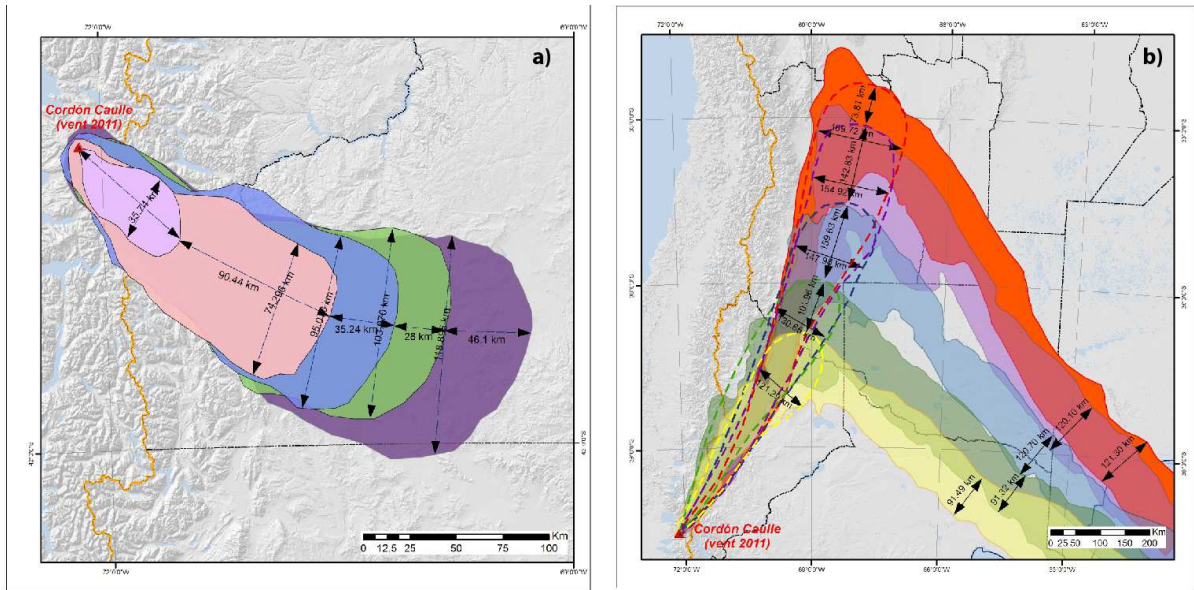


Fig. 10 Downwind and crosswind extension of the volcanic clouds developed on **a)** June 4, 2011 and **b)** June 6, 2011 as observed from the GOES satellite images for the time interval 18:45-20:15 UTC and 12:45-19:45 UTC respectively (total measurement uncertainty includes pixel size of these GOES images, i.e. ~2 km, and definition of cloud boundaries, i.e. ~5km). On June 6 two distinct clouds developed: one moving towards NE and one moving towards SE.

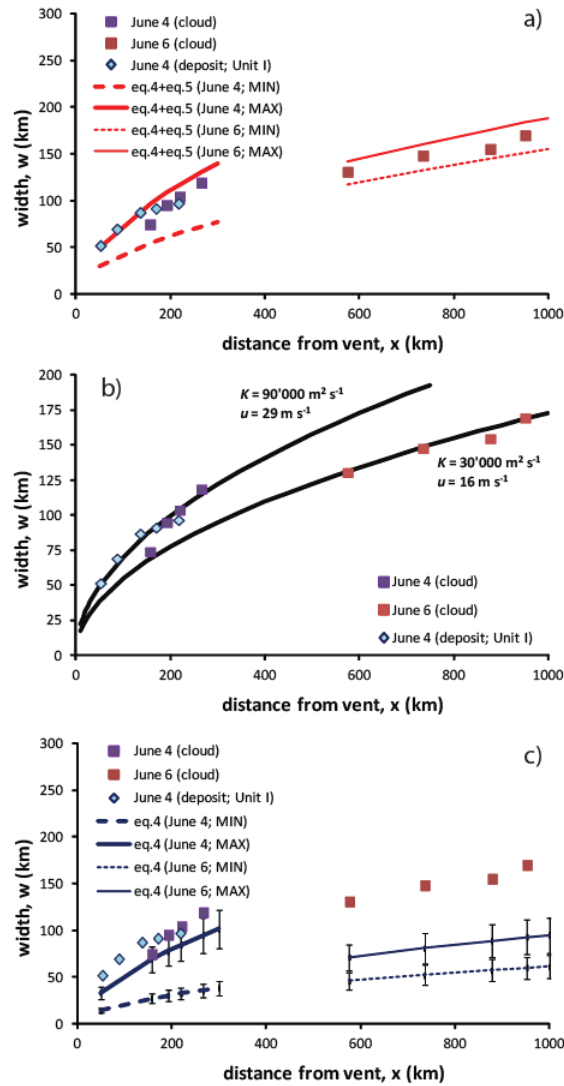


Fig. 11 Variation of downwind distance from vent versus width for: i) volcanic clouds developed on both June 4 and 6 (NE cloud) as observed from satellite images (violet and red squares, respectively; from Fig. 10) and ii) 1 kg m⁻² isoline of Unit I (blue diamonds; Supporting Information) described as:

a) gravitational spreading plus turbulent diffusion (for a best-fit diffusion coefficient of 9,000 m² s⁻¹). Dashed and solid lines are associated with minimum and maximum values of volumetric flow rate (Q) at the neutral buoyancy level, respectively, related to variable plume height and atmospheric conditions, i.e. 0.5-4.3x10⁹ m³ s⁻¹ (for the June 4 event) and 3.5-8.6x10⁸ m³ s⁻¹ (for the June 6 event) (as calculated with the model of *Degruyter and Bonadonna* [2012]);

b) turbulent diffusion (eq. 5) for best-fit diffusion coefficients K (m² s⁻¹) and wind velocity u (m s⁻¹) averaged between neutral buoyancy level and total plume height and between the volcano location and the maximum extension of the observed cloud for June 4 and June 6 (indicated next to best-fit lines); for simplicity, an average wind velocity of 29 m s⁻¹ for minimum and maximum plume height of June 4th was considered;

c) gravitational spreading (eq. 4 considering $\lambda=0.8$ and $N=0.01$ s⁻¹; see *Bonadonna and Phillips* [2003] for more details). Vertical bars indicate a 20% uncertainty on the calculated width in relation to the cloud geometry (see *Bonadonna and Phillips* [2003] for more details).

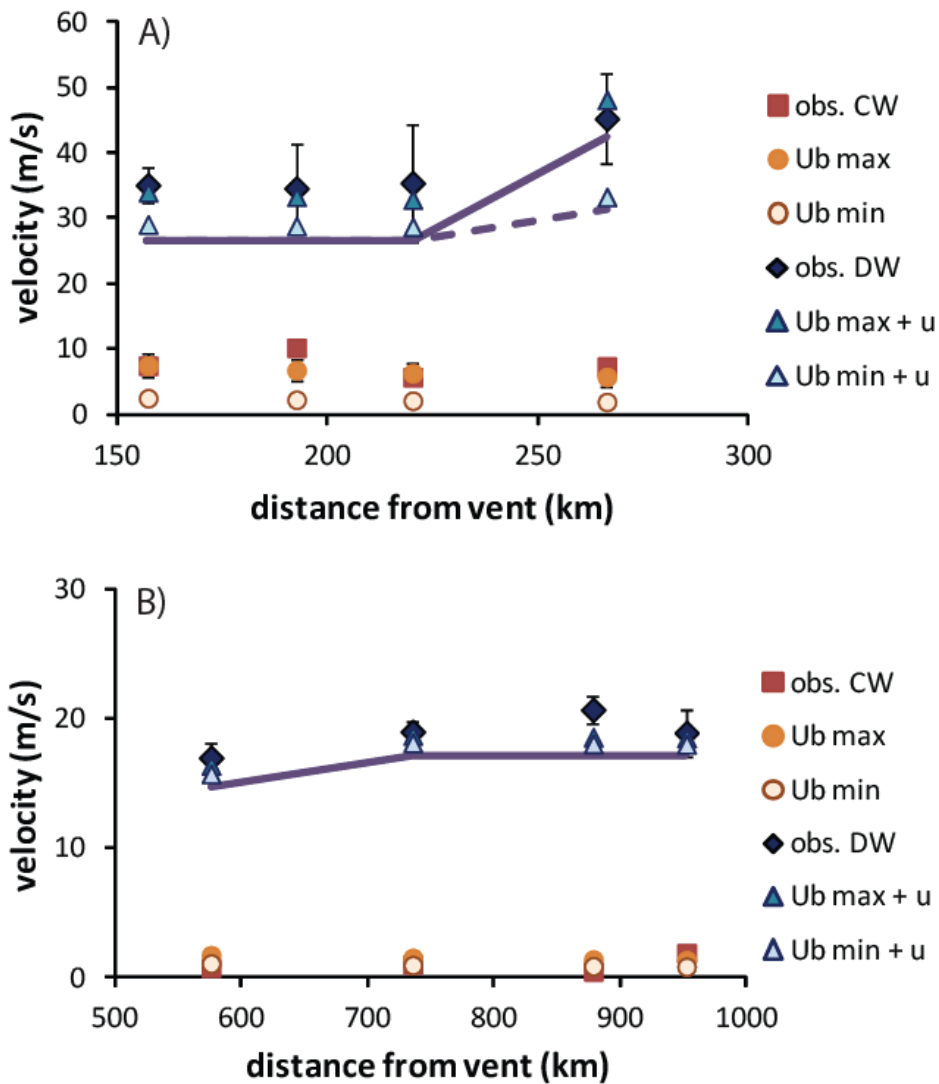


Fig. 12 Variation of spreading velocity in the downwind (blue diamonds) and crosswind (red squares) directions at various distances from vent for: **a)** June 4, 2011 (observations between 18:45 and 20:15 UTC) and **b)** June 6, 2011 (observations between 12:45 and 19:45 UTC). Solid and dashed lines indicate the wind velocity u (m s^{-1}) at each distance from vent for minimum and maximum plume height (see Fig. 5 and Supporting Information for plume height data; only one height observation is available for June 6). Wind data are averaged between the neutral buoyancy level and total plume height for each cloud position. Circles and triangles indicate respectively the spreading velocity due to buoyancy (u_b , as calculated for minimum and maximum values of Q from eq. 6 considering $\lambda=0.8$ and $N=0.01 \text{ s}^{-1}$) and the downwind velocity calculated as a combination between u_b and u . Q values used in eq. 6 are described in caption of Fig. 11. Vertical bars indicate the uncertainty associated with the observed velocity derived from an average cumulative error of $\pm 7\text{km}$ on the downwind and crosswind lengths (see Fig. 10 for more details). A 25% uncertainty on the calculated minimum and maximum cloud-spreading velocity due to buoyancy (u_b) is also shown (as estimated by *Bonadonna and Phillips* [2003] in relation to the cloud geometry).